



Illuminating Low Surface Brightness Galaxies with the Hyper Suprime-Cam Survey

Johnny P. Greco¹ , Jenny E. Greene¹, Michael A. Strauss¹ , Lauren A. MacArthur¹, Xavier Flowers^{1,2}, Andy D. Goulding¹, Song Huang³ , Ji Hoon Kim⁴ , Yutaka Komiyama^{5,6}, Alexie Leauthaud³ , Lukas Leisman⁷, Robert H. Lupton¹ , Cristóbal Sifón¹ , and Shiang-Yu Wang⁸

¹ Department of Astrophysical Sciences, Princeton University, Princeton, NJ 08544, USA; jgreco@astro.princeton.edu

² Florida Institute of Technology 150 W. University Blvd., Melbourne, FL 32901, USA

³ Department of Astronomy and Astrophysics, University of California, Santa Cruz, 1156 High Street, Santa Cruz, CA 95064 USA

⁴ Subaru Telescope, National Astronomical Observatory of Japan, 650 N. Aohoku Pl., Hilo, HI 96720, USA

⁵ National Astronomical Observatory of Japan, 2-21-1 Osawa, Mitaka, Tokyo 181-8588, Japan

⁶ Department of Astronomy, School of Science, Graduate University for Advanced Studies (SOKENDAI), 2-21-1, Osawa, Mitaka, Tokyo 181-8588, Japan

⁷ Department of Physics and Astronomy, Valparaiso University, Valparaiso, IN 46383, USA

⁸ Institute of Astronomy and Astrophysics, Academia Sinica, P.O. Box 23-141, Taipei 106, Taiwan

Received 2017 August 20; revised 2018 March 4; accepted 2018 March 16; published 2018 April 20

Abstract

We present a catalog of extended low surface brightness galaxies (LSBGs) identified in the Wide layer of the Hyper Suprime-Cam Subaru Strategic Program (HSC-SSP). Using the first ~ 200 deg 2 of the survey, we have uncovered 781 LSBGs, spanning red ($g - i \geq 0.64$) and blue ($g - i < 0.64$) colors and a wide range of morphologies. Since we focus on extended galaxies ($r_{\text{eff}} = 2.5''\text{--}14''$), our sample is likely dominated by low-redshift objects. We define LSBGs to have mean surface brightnesses $\bar{\mu}_{\text{eff}}(g) > 24.3$ mag arcsec $^{-2}$, which allows nucleated galaxies into our sample. As a result, the central surface brightness distribution spans a wide range of $\mu_0(g) = 18\text{--}27.4$ mag arcsec $^{-2}$, with 50% and 95% of galaxies fainter than 24.3 and 22 mag arcsec $^{-2}$, respectively. Furthermore, the surface brightness distribution is a strong function of color, with the red distribution being much broader and generally fainter than that of the blue LSBGs, and this trend shows a clear correlation with galaxy morphology. Red LSBGs typically have smooth light profiles that are well characterized by single-component Sérsic functions. In contrast, blue LSBGs tend to have irregular morphologies and show evidence for ongoing star formation. We cross-match our sample with existing optical, H I, and ultraviolet catalogs to gain insight into the physical nature of the LSBGs. We find that our sample is diverse, ranging from dwarf spheroidals and ultradiffuse galaxies in nearby groups to gas-rich irregulars to giant LSB spirals, demonstrating the potential of the HSC-SSP to provide a truly unprecedented view of the LSBG population.

Key words: galaxies: dwarf – galaxies: general

Supporting material: machine-readable tables

1. Introduction

Low surface brightness galaxies (LSBGs) are a significant component of the galaxy population (McGaugh et al. 1995a; Dalcanton et al. 1997a), which spans a broad range of galaxy properties and environments (e.g., Bothun et al. 1987; McGaugh et al. 1995b; Impey et al. 1996; O’Neil et al. 1997; Beijersbergen et al. 1999; Zucker et al. 2006; McConnachie 2012; van Dokkum et al. 2015). Furthermore, many of the most pressing problems currently facing the Λ cold dark matter (Λ CDM) paradigm were discovered (and may be resolved) through studies of galaxies in the low-luminosity and/or LSB regime (e.g., Kauffmann et al. 1993; Klypin et al. 1999; Moore et al. 1999; Boylan-Kolchin et al. 2011). Despite the importance of LSBGs (for a review of classical LSBGs, see Bothun et al. 1997; Impey & Bothun 1997), their defining characteristic—central surface brightnesses that are fainter than the night sky—makes them difficult to detect and study, which has led to their underrepresentation in previous optical surveys, thus biasing our view of the full galaxy population (Disney 1976).

Indeed, uncovering the distribution of galaxies at ever-lower surface brightnesses remains an active area of research (e.g., Impey et al. 1988; McGaugh 1996; Blanton et al. 2005; Muñoz et al. 2015; van der Burg et al. 2016; Román & Trujillo 2017a). Modern wide-field surveys such as the Sloan Digital Sky

Survey (SDSS; York et al. 2000) have enabled statistical studies of large samples of LSBGs down to central surface brightnesses of $\mu_0(B) \sim 24$ mag arcsec $^{-2}$ (e.g., Zhong et al. 2008; Rosenbaum et al. 2009; Galaz et al. 2011), and fainter limits are continuously being reached through advances in observing strategies and data reduction (e.g., Blanton et al. 2011; Ferrarese et al. 2012; Duc et al. 2015; Fliri & Trujillo 2016; Trujillo & Fliri 2016). Pushing to still lower surface brightnesses, optical and H I surveys have been combined to detect and characterize populations of gas-rich LSBGs (e.g., Du et al. 2015; Leisman et al. 2017).

Small robotic telescopes optimized for LSB science (e.g., Martínez-Delgado et al. 2010; Abraham & van Dokkum 2014; Javanmardi et al. 2016) have recently joined the search for LSBGs, which notably resulted in the discovery of a significant population of red, ultra-LSB galaxies within the Coma Cluster (Koda et al. 2015; van Dokkum et al. 2015; Yagi et al. 2016). With central surface brightnesses $\mu_0(g) \gtrsim 24$ mag arcsec $^{-2}$ and effective radii $r_{\text{eff}} \gtrsim 1.5$ kpc, these so-called ultradiffuse galaxies (UDGs) are remarkable in that they have stellar masses similar to dwarf galaxies spread over diameters comparable to that of the Milky Way. While UDG-like objects have been known to exist for decades (e.g., Sandage & Binggeli 1984), their unexpected abundance in the Coma Cluster has reignited the search for LSBGs, leading to the discovery of UDGs in

environments ranging from dense galaxy clusters to the field (Mihos et al. 2015; Martínez-Delgado et al. 2016; Merritt et al. 2016; Bellazzini et al. 2017; Leisman et al. 2017; Román & Trujillo 2017b; van der Burg et al. 2017).

In the Λ CDM framework, LSBGs naturally arise within dark matter halos with high angular momentum (Dalcanton et al. 1997b). Therefore, measurements of their number densities and kinematic properties can provide powerful tests of cosmological models (e.g., Ferrero et al. 2012; Papastergis et al. 2015). For UDGs specifically, their number density as a function of environment can be explained if they preferentially form in dwarf-mass halos ($M_{\text{virial}} \sim 10^{10} M_{\odot}$) with higher-than-average angular momentum (Amorisco & Loeb 2016), a view that is consistent with recent weak-lensing (Sifón et al. 2018) and HI (Leisman et al. 2017) observations. Alternatively, van Dokkum et al. (2015) suggested that UDGs may be “failed” galaxies, with external mechanisms such as gas stripping and/or extreme feedback processes suppressing the growth of normal stellar populations at a given halo mass. This scenario also appears to be viable for at least some fraction of UDGs (e.g., van Dokkum et al. 2016). Of course, it is crucial to understand how UDGs fit into the broader context of the LSBG population and whether these galaxies have different formation paths as a function of physical properties (e.g., size, mass, and color) and environment.

The new generation of wide-field optical imaging surveys, such as the Dark Energy Survey (Dark Energy Survey Collaboration et al. 2016), the Kilo-Degree Survey (de Jong et al. 2015), our ongoing Hyper Suprime-Cam Subaru Strategic Program (HSC-SSP; Aihara et al. 2018a), and ultimately the Large Synoptic Survey Telescope (LSST; Ivezić et al. 2008), will extend our census of the galaxy population to lower surface brightnesses than has previously been possible over large areas of the sky. Although it will require dedicated LSB-optimized reduction and analysis efforts, these surveys will produce statistical samples of LSBGs that span all halo environments, opening a new window into their formation and evolution and providing ideal systems to test the predictions of Λ CDM.

In this work, we present initial results from our search for LSBGs with the HSC-SSP. We focus on angularly extended (and therefore primarily low- z) LSBGs. We define and select LSBGs to have g -band mean surface brightnesses within their circularized effective radii $\bar{\mu}_{\text{eff}}(g) > 24.3 \text{ mag arcsec}^{-2}$, which is equivalent to $\mu_0(g) > 23.5 \text{ mag arcsec}^{-2}$ for a Sérsic surface brightness profile (Sérsic 1968) with Sérsic index $n = 0.8$.

The paper is organized as follows. In Section 2, we discuss the Wide layer of the HSC-SSP, on which our study is based. We then describe our LSBG source detection pipeline in Section 3. In Section 4, we present our galaxy sample. In Section 5, we cross-match our catalog with previous work to gain insight into the span of physical properties within our sample. We conclude with a summary and outlook in Section 6. In addition, we give examples of nongalactic LSB sources detected by our pipeline in the Appendix.

For all relevant calculations, we assume a standard cosmology with $H_0 = 70 \text{ km Mpc}^{-1}$, $\Omega_m = 0.3$, and $\Omega_{\Lambda} = 0.7$. All magnitudes presented in this paper use the AB system (Oke & Gunn 1983). Unless stated otherwise, we correct for Galactic extinction using the $E(B - V)$ values from the dust map of Schlegel et al. (1998) and the recalibration from Schlafly & Finkbeiner (2011).

2. The Wide Layer of HSC-SSP

Our search is based on the first $\sim 200 \text{ deg}^2$ from the Wide layer of the HSC-SSP (internal data release S16A), an ambitious 300-night imaging survey using the Hyper Suprime-Cam (Miyazaki et al. 2018) on the 8.2 m Subaru Telescope. Upon completion, the Wide layer will cover $\sim 1400 \text{ deg}^2$ in five broad bands ($grizy$), achieving a depth of $i \sim 26 \text{ mag}$ (5σ point-source detection) with a median seeing of $0.6''$. An overview of the full survey design is given in Aihara et al. (2018a), and the first public data release, which covers $\sim 100 \text{ deg}^2$, is described in Aihara et al. (2018b). Here, we will briefly summarize some key aspects of the survey that are relevant to our search.

The HSC-SSP data are processed using an open-source software package, *hscPipe*, which builds on the pipeline being built for the LSST Data Management system⁹ (Axelrod et al. 2010; Jurić et al. 2015). The software pipeline is described in detail by Bosch et al. (2018). For our search, we work with the fully reduced, sky-subtracted co-add images. *hscPipe* divides these images into equi-area rectangular regions called *tracts*, which are predefined as iso-latitude tessellations. Each tract covers 1.7 deg^2 of sky, and neighboring tracts have an overlap of $\sim 1'$ near the equatorial fields. The tracts are further divided into 9×9 grids of *patches*. Each patch is composed of 4200×4200 pixels ($\sim 12'$ on a side), with 100-pixel ($\sim 17''$) overlaps between adjacent patches.

Since we are searching for galaxies that are by definition fainter than the night sky, the quality of the sky subtraction is important for our search. As described in Bosch et al. (2018), *hscPipe* estimates the sky on a CCD-by-CCD basis by averaging pixels in 128×128 pixel grids, where pixels belonging to detected objects are ignored. The average pixel values are then fit with a sixth-order two-dimensional Chebyshev polynomial, which is used to subtract a smooth, slowly varying flux distribution from the image. This algorithm is known to oversubtract the background around large extended objects on the sky ($> 1'$) such as bright, nearby galaxies (Aihara et al. 2018b). Therefore, our LSBG search will likely be biased against detecting galaxies projected within a few effective radii of such objects. Implementing a custom sky-subtraction algorithm across the entire HSC-SSP footprint is beyond the scope of this paper, but we note that a new and improved sky-subtraction algorithm that uses the entire HSC field of view has been developed and will be implemented in future HSC-SSP data releases.

We carry out our search on a patch-by-patch basis; in total, we search 11,176 patches, which, after accounting for overlaps and masking, reduces to $\sim 200 \text{ deg}^2$. We restrict our search to patches that have been observed to the full Wide layer depth in g , r , and i as of 2016 May. We note that we only work with gri , since requiring all five bands ($grizy$) at the full Wide layer depth would limit our survey area. Studies using the full spectral range are forthcoming.

3. Source Detection Pipeline

Currently, *hscPipe* is optimized to identify faint, small (several arcseconds in radius) objects, which are characteristic of galaxies in the distant universe—identifying these objects is one of the main drivers of the HSC-SSP. Unfortunately, this is not optimal for the detection of extended LSBGs; *hscPipe*

⁹ <http://dm.lsst.org>

tends to decompose these single extended systems into a set of child objects, so-called “shredding.” This problem also affects the measurements of bright, nearby galaxies, which often have significant substructure that leads to overdeblending (Aihara et al. 2018b). Galaxy shredding is well known to exist in SDSS (e.g., Kniazev et al. 2004; Fukugita et al. 2007), but it is much more pronounced at the depths of the HSC-SSP.

A typical extended LSBG in the current HSC-SSP catalog will be shredded into many ($\gtrsim 10$) child objects and a parent object centered on the brightest peak within the source footprint, which will not necessarily be associated with the luminosity- or position-weighted center of the galaxy. Furthermore, the faint integrated light from LSBGs is often dominated by background/foreground objects that may be assigned as the galaxy’s center if they fall within the extended LSB footprint. As a result, shape and surface brightness measurements of LSBGs in the HSC-SSP catalog are often spurious, making it difficult to construct a robust selection of such objects. To address this issue, we have developed a custom pipeline to perform our search.

Our source extraction pipeline is open-source¹⁰ and is currently under active development. Our software is based primarily on the LSST codebase, which provides a powerful suite of tools for optical/near-infrared source detection and photometry. We additionally use SExtractor¹¹ (Bertin & Arnouts 1996) in our pipeline’s final detection step to estimate initial galaxy parameters for selection and *imfit*¹² (Erwin 2015) to refine our parameter estimates.

In this section, we describe the major steps of our pipeline. As noted in Section 2, our search is carried out using the co-add images from the Wide layer of HSC-SSP, which have been fully reduced (including sky subtraction) by *hscPipe*. We perform our detection in the *i* band (typical seeing $\sim 0''.6$) and require that all sources also be detected in the *g* band (typical seeing $\sim 0''.7$) to reduce the number of false positives associated with optical artifacts such as ghosts or scattered light from bright stars. The image-processing steps described below are applied to *i*-band images unless stated otherwise.

For the reader only interested in the broad outline of our pipeline, the major steps (which we describe in detail below) are the following:

1. *Remove bright sources and associated diffuse light.* LSB light associated with nearby, bright sources can mimic the signal of our objects of interest. We detect these sources using multiple levels of thresholding and replace their footprints with sky noise.
2. *Source extraction.* We smooth the “cleaned” images produced by the previous step with a fairly large Gaussian kernel (FWHM = $1''$) and extract sources using SExtractor that are composed of 100 or more connected pixels (1 pixel = $0''.168$) with a low detection threshold of 0.7σ per pixel. This produces a sample of $\sim 7 \times 10^6$ unique sources, the vast majority of which are small and faint.
3. *Initial sample selection.* We then make selection cuts on the parameters measured by SExtractor. By far the most powerful cut we apply is $r_{1/2} > 2''.5$, where $r_{1/2}$ is the half-light radius. This cut alone reduces our sample to

20,838 sources. We also apply reasonable color cuts based on SExtractor aperture photometry.

4. *Galaxy modeling.* We model the two-dimensional surface brightness profiles of the remaining candidates using *imfit*. We then make a second selection based on the mean (*g*-band) surface brightness within the circularized effective radius $\bar{\mu}_{\text{eff}}(g)$ as measured by *imfit*. In addition, we remove likely astrophysical false positives by comparing the measurements of SExtractor and *imfit*. This step reduces our sample to 1521 candidate LSBGs.

5. *Visual inspection.* We visually inspect all the remaining candidates and remove any obvious false positives, which are dominated by the blending of point-like sources with background/foreground diffuse light (e.g., from a nearby bright star, massive low- z galaxy, or Galactic cirrus), which were not removed by step 1. After this step, we are left with a final sample of 781 LSBGs.

3.1. Step 1: Bright Sources and Associated Diffuse Light

The first step of our pipeline is to remove bright sources and their associated diffuse light (e.g., the LSB outskirts of giant elliptical galaxies). While the former may in principle be removed at the catalog level, the latter tends to be shredded into individual objects whose measured properties are very similar to our objects of interest. This problem is often addressed by using multiple SExtractor runs with different configurations that are optimized to detect high surface brightness (HSB) and LSB sources separately (e.g., Rix et al. 2004; Barden et al. 2012; Prescott et al. 2012). The resulting catalogs can then be cross-matched to build a final, more complete catalog. One benefit of using the LSST codebase is that we have complete control of each image-processing step. This allows us to perform multiple levels of thresholding without having to build a full catalog at each level, as is necessary when using multiple SExtractor runs.

For each patch ($\sim 12''$ on a side; see Section 2), we use the following steps to remove bright sources and their associated diffuse light. We start by smoothing the image with a circular Gaussian matched to the rms width of the point-spread function (PSF). Image convolution maximizes the ratio of a source’s peak signal to the local noise level (e.g., Irwin 1985; Akhlaghi & Ichikawa 2015), and the PSF scale is formally optimal for the idealized case of detecting isolated point sources (Bosch et al. 2018). Additionally, this is the smallest scale at which we can detect real astrophysical sources, so it reduces the impact of pixels with high noise fluctuations. Next, we find very bright sources by flagging all pixels that are at least 28σ above the global background level for each patch; for a typical patch, this corresponds to the brightest $\sim 2\%$ of all pixels. The background and its variance are estimated using several iterations of sigma clipping. We then identify LSB structures as collections of 20 or more pixels that are at least 3σ above the background level; this LSB image thresholding is carried out on the identical image as the previous HSB thresholding. Finally, we associate LSB structures with bright sources if more than 15% of their pixels are above the high threshold used during the first round of thresholding.

The numbers presented above (28σ , 3σ , and 15%) were chosen after many iterations of trial and error. There is a trade-off between aggressively removing all LSB pixels that are physically associated with HSB sources and inadvertently

¹⁰ <https://github.com/johnnygreco/hugs>

¹¹ <https://www.astromatic.net/software/sextractor>

¹² <http://www.mpe.mpg.de/~erwin/code/imfit/>

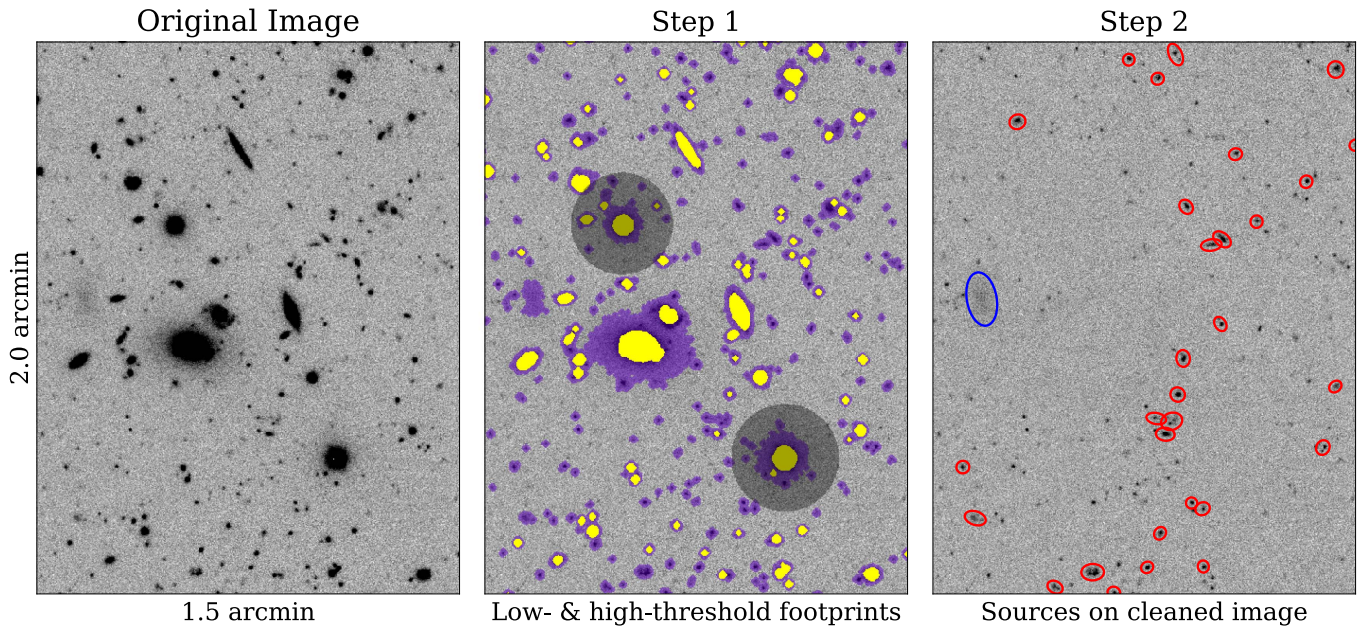


Figure 1. HSC-SSP *i*-band images demonstrating the first two steps of our pipeline. We show a small section of a single patch for clarity. The original image is shown in the left panel, with the dimensions of the cutouts indicated on the axes. In the middle panel, we demonstrate how we find and remove bright sources and their associated diffuse light using multiple levels of thresholding. We show overlays of the high-threshold footprints (yellow), which identify bright sources, and the low-threshold footprints (purple), which identify the associated diffuse light. The two shaded circles are from the bright-object mask supplied by *hscPipe* (Coupon et al. 2018; Mandelbaum et al. 2018). We replace a low-threshold footprint with sky noise if more than 15% of its pixels are above the high threshold value. We also replace the *hscPipe* bright-object mask with sky noise, producing a final “cleaned” image. In the right panel, we show ellipses on sources identified within the cleaned image. Note the large LSB source with the blue ellipse, which is the only detected object that passes our size cut (see Section 3.3). The faint sources apparent in the image that were not detected (i.e., those without an ellipse) had too few connected pixels above the required threshold.

removing LSBGs that happen to be near (in projection or physically) HSB sources. The middle panel of Figure 1 shows an example image with low- (purple) and high-threshold (yellow) footprints overlaid.

We generate a final bright-object mask by taking the union of the source footprints (bright sources + associated diffuse light) and the bright-object masks provided by *hscPipe*—we use an early version of the masks called *Sirius* (Mandelbaum et al. 2018), which has since been superseded by *Arcturus* (Coupon et al. 2018). The two shaded circles in the middle panel of Figure 1 show bright objects that were masked by *hscPipe*. We then replace masked pixels with sky noise generated from a Gaussian distribution with zero mean (the images have been background subtracted by *hscPipe*) and standard deviation equal to the rms pixel value. We use the same mask to perform noise replacement of pixels in the *g*-, *r*-, and *i*-band images. An example “cleaned” *i*-band image is shown in the right panel of Figure 1.

3.2. Step 2: Source Extraction

The previous step of our pipeline produces “cleaned” images for each patch, where bright sources and their associated diffuse light have been replaced by sky noise. Next, we perform source extraction and estimate an initial set of galaxy parameters. While it would be possible to use the LSST codebase for this step, we found that the currently implemented shape-measurement algorithms tend to fail for very LSB, extended targets. We therefore use SExtractor for this task, which has been well tested in the LSB regime (e.g., van der Burg et al. 2016; Yagi et al. 2016).

We perform our detections in the *i* band but require that they also be detected in the *g* band to reduce contamination from optical artifacts. Before detection, we smooth the images with a Gaussian kernel with $\text{FWHM} = 1''$ (nearly twice the typical *i*-band seeing) to boost our LSB sensitivity. We experimented with larger kernel sizes up to $\text{FWHM} = 6''$ but found that the increase in contamination from blends was not worth the gain in sensitivity. Blends of faint galaxies and/or distant galaxy groups are a major source of contamination for any deep diffuse-galaxy search (e.g., Koda et al. 2015; Sifón et al. 2018). The faintness of these sources means that they will not be masked by the previous step of our pipeline, and if detected as single objects, their sizes will be biased high and their central surface brightnesses will be biased low, making them look like the objects we are searching for.

Although we are working on background-subtracted images, we re-estimate the *local* background using a mesh size of 128 pixels $\approx 22''$. We use a low detection threshold of 0.7σ per pixel above the local background level; at lower thresholds, contamination (e.g., from the LSB outskirts of bright galaxies or diffuse light from stars) becomes too overwhelming. We require that all detections be composed of at least 100 contiguous pixels. We require such large footprints because of our low detection threshold and because we are primarily interested in finding very extended LSBGs. For HSC-SSP images, an area of 100 pixels corresponds to a circular region of radius $\sim 1\text{--}2$ times the FWHM of the PSF.

We perform aperture photometry (to be used for selection) in the *i* band using an aperture size of 2.5 times (the default value for SExtractor AUTO parameters) the Kron radius (Kron 1980). To measure colors (again, only for selection purposes), we

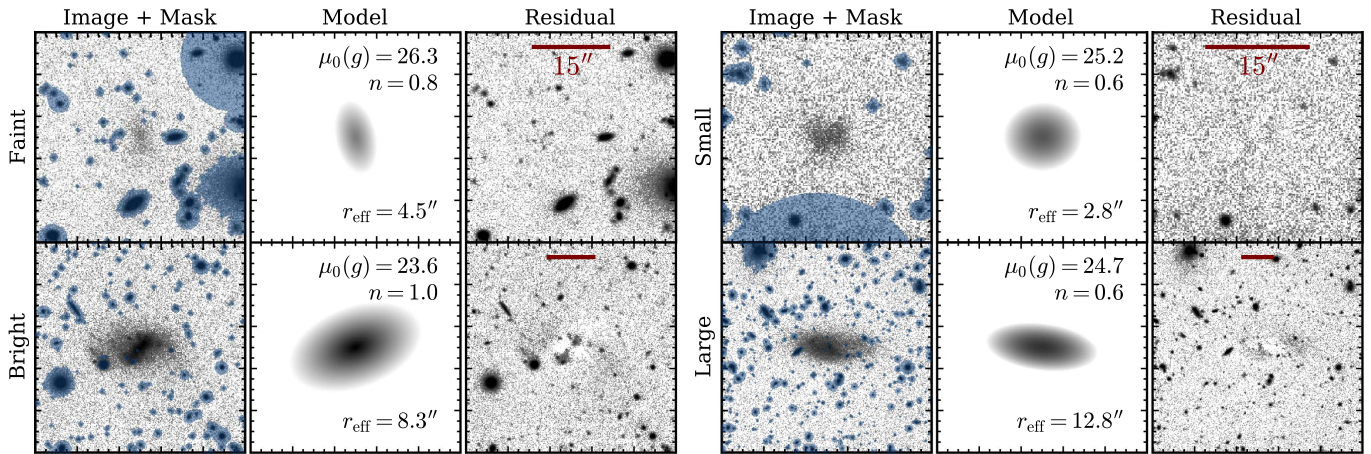


Figure 2. Example Sérsic function fitting results. We show i -band cutouts that are $12 \times r_{1/2}$ on a side, where $r_{1/2}$ is the half-light radius of the associated galaxy, as measured by SExtractor (i.e., not r_{eff} , which is measured by *imfit*). The images are shown with a logarithmic stretch. The left columns show the original galaxy images with overlays of the object masks, the middle columns show the best-fit models with the main model parameters indicated for each galaxy, and the right columns show the residual images. We show results for four galaxies from our final sample, which are faint (top left), bright (bottom left), small (top right), and large (bottom right) with respect to the full sample. The angular scales are indicated at the top of each residual image.

apply the i -band apertures to the g - and r -band images—the photometry is forced.

For a typical patch ($\sim 12' \times 12'$ region of sky), the above procedure generates a catalog of ~ 900 objects, most of which can be rejected owing to their small angular size. In the rightmost panel of Figure 1, the blue ellipse shows the detection of an ultra-LSB source. Note its large angular size compared to the other sources. In total, this step generated a catalog of $\sim 7 \times 10^6$ unique sources after removing duplicate detections due to overlaps between patches.

3.3. Step 3: Initial Sample Selection

We now seek a set of selection cuts that will reduce our sample to a manageable size for more detailed galaxy modeling. To accomplish this, we use size and color measurements from SExtractor. In particular, we keep sources that have i -band half-light radii, as measured by SExtractor via the `FLUX_RADIUS` parameter, within $2.5'' < r_{1/2} < 20''$. The lower bound is due to our interest in extended galaxies; for objects within $z \sim 0.01$ –0.03 (approximate range of our closest objects with known redshifts; see Section 5), $2.5''$ corresponds to $r_{1/2} \sim 0.5$ –1.5 kpc. Since we perform our search on a patch-by-patch basis, the upper bound is set by the $17''$ overlap between patches (see Section 2). We inspected detections larger than this scale, and they are rare and generally spurious. The minimum radius cut is by far our most powerful selection criterion, reducing the number of sources from 7×10^6 to 20,838.

We further require the SExtractor-measured colors to be within the color box defined by

$$\begin{aligned} -0.1 < g - i < 1.4, \\ (g - r) > 0.7 \cdot (g - i) - 0.4, \text{ and} \\ (g - r) < 0.7 \cdot (g - i) + 0.4. \end{aligned}$$

These color requirements were determined empirically using our full catalog of objects and primarily remove spurious detections due to optical artifacts detected in all bands and blends of high-redshift galaxies. This color box is conservative with respect to what we expect from red and blue LSBGs (e.g., Geha et al. 2017; Román & Trujillo 2017a, 2017b), as well as

with respect to reasonable assumptions about stellar populations (as we show in Section 4.1). This cut reduces our sample to 14,069 sources.

3.4. Step 4: Galaxy Modeling

For the LSBG candidates that remain after the selection cuts of Section 3.3, we next refine our galaxy parameter measurements using *imfit*. For each candidate, we extract a square cutout image that is $12 \times r_{1/2}$ on a side and centered on the centroid determined by SExtractor. The cutout images have been fully reduced by *hscPipe* (including background subtraction). We mask objects that are not associated with the galaxy’s smooth light profile using a combination of the *hscPipe* bright-object masks and an automatically generated object mask using *sep*¹³ (Barbary 2016), a source extraction Python package based on the core algorithms of SExtractor. We run our masking software on all bands individually and take the union to form a final mask. When performing the fits, we use the variance images and PSF measurements provided by *hscPipe*. We model the surface brightness distribution as a two-dimensional, PSF-convolved Sérsic function. We first perform fits in the i band, which by design typically has the best-quality data for HSC-SSP. To measure colors, we fit the g - and r -band images with all parameters except for the amplitude fixed at their i -band values; note that this assumes no color gradients. In Figure 2, we show example fit results for LSBGs that are faint, bright, small, and large with respect to the median of our full sample.

Since the characteristic central surface brightness of our sample is much fainter than the brightness of the night sky, the measured galaxy parameters are sensitive to the assumed sky value, which is estimated by *hscPipe*. We quantify the impact of this uncertainty by performing the above fitting procedure a second time with an additional free parameter for the sky value in each cutout. We then compare the best-fit total magnitudes, central surface brightnesses (μ_0), Sérsic indices (n), effective radii (r_{eff}), and ellipticities (ϵ) with those of our previous models where the sky is fixed. We take the rms of the distributions of the parameter differences to be the statistical

¹³ <https://sep.readthedocs.io>

uncertainties associated with the sky estimate. For a small fraction of objects (<3%), varying the sky value leads to significant differences in the parameters (particularly the effective radii). These objects tend to be either very LSB and in close proximity to a bright star or low- z galaxy or multicomponent systems that are less well described by a single Sérsic model; we sigma clip the distributions at 5σ to remove these rare cases before calculating the rms values. We add these values in quadrature with the formal fitting uncertainties estimated by *imfit* to derive final uncertainties, which range from $\sim 10\%$ to 30% in effective radii and from ~ 0.2 to 0.4 mag in total magnitudes.

With refined galaxy parameter estimates from *imfit*, we next make a second set of selection cuts. We keep candidates that satisfy the following:

1. Effective radius, measured along the major axis, $r_{\text{eff}} > 2.5''$, since our focus is on extended LSBGs.
2. g -band mean effective surface brightness within the circularized effective radius $24.3 < \bar{\mu}_{\text{eff}}(g) < 28.8$. This is equivalent to requiring central surface brightness within $23.5 < \mu_0(g) < 28$ for a Sérsic profile with $n = 0.8$. Low-mass LSBGs typically have $n \sim 1$ (e.g., Geha et al. 2006; Román & Trujillo 2017a). Our choice of $n = 0.8$ is more inclusive than an exponential profile. We cut on $\bar{\mu}_{\text{eff}}(g)$ rather than $\mu_0(g)$ to allow nucleated galaxies into our sample.
3. Ellipticity $\epsilon < 0.7$. This cut removes nearly edge-on, high-redshift galaxies, whose surface brightnesses appear low owing to cosmological dimming, as well as some galaxy blends and linear optical artifacts that tend to have high ellipticity. While in principle this biases our sample to some degree, we find that most of our candidates are far less elongated.
4. We remove likely astrophysical false positives (e.g., blends and residual light from a bright galaxy that was not completely masked) by comparing the parameters measured by SExtractor and *imfit*. Specifically, we require that the difference between the centroids be less than $4''$ and the difference between SExtractor's MAG_AUTO parameter and the total magnitude measured by *imfit* be less than 1 mag in all bands (*gri*).

The above selection produced a catalog of 1521 LSBG candidates.

3.5. Step 5: Visual Inspection

We visually inspect all of the LSBG candidates from the previous four steps and remove any remaining false positives; $\sim 50\%$ of the objects are eliminated by this step. The dominant false positives are due to blends of point-like sources superposed on extended halos of diffuse light (e.g., from a bright star, giant low- z galaxy, or Galactic cirrus). We can reduce our contamination to $\sim 25\%$ by being more aggressive during the masking in step 1; however, this comes at the cost of reducing our sample size by a factor of 2. We choose to accept the extra contamination in favor of better completeness.

The first two authors independently performed the visual inspection. We note that it is difficult to consistently distinguish between tidally disturbed dwarfs and tidal debris ejected during galaxy interactions (see, e.g., the Appendix and Greco et al. 2018). To (at least slightly) reduce the impact of the

inevitable subjectivity in this process, we only keep sources that we both flagged as a galaxy.

In summary, we use SExtractor to build an initial catalog of $\sim 7 \times 10^6$ sources. We then make cuts based on size and color, as measured by SExtractor, which reduces our sample to 14,069 objects. We model each of these remaining sources using *imfit*, and we cut on the resulting parameters to yield a sample of 1521 LSBG candidates. Finally, we visually inspect the candidates, producing a final catalog of 781 LSBGs, which will be the focus of the remainder of the paper.

4. The Galaxy Sample

We have run our source detection pipeline (Section 3) on the first ~ 200 deg 2 of the Wide layer of the HSC-SSP, which will grow to 1400 deg 2 upon survey completion. The power of this survey is that it is simultaneously wide, deep, and sharp, allowing for a homogeneous study of LSB sources in environments ranging from the field to dense galaxy clusters. Indeed, our search has uncovered a rich diversity of LSB phenomena, including LSBGs, tidal debris from galaxy interactions, and scattered light from dust in the Milky Way (Galactic cirrus). See the Appendix for representative examples of the latter two types of LSB sources, which can be significant contaminants in searches for LSBGs.

The primary goal of this work is to identify and characterize extended LSBGs. Our final sample consists of 781 galaxies, which span a wide range of colors, morphologies, and environments. In this section, we separate our sample into red and blue subsamples and present their observed properties. We publish our full LSBG catalog, the contents of which are summarized in Tables 1 and 2, in machine-readable format.

4.1. Colors

The optical colors of galaxies reveal their dominant stellar populations and thus correlate strongly with galaxy morphology, leading to the well-known separation of galaxies into red and blue sequences (e.g., Strateva et al. 2001; Blanton & Moustakas 2009). While large-scale surveys such as SDSS have enabled detailed studies of the color distribution of galaxies down to $\bar{\mu}_{\text{eff}}(r) \sim 24.5$ mag arcsec $^{-2}$ (e.g., Baldry et al. 2004), less is known about the color distribution at lower surface brightnesses. Classical disk LSBGs are known to span blue to red colors (O’Neil et al. 1997). Blue colors are generally associated with spiral or irregular systems, whereas red colors are indicative of spheroids or ellipticals (Mateo 1998), with quenched galaxies being found almost exclusively in association with massive host systems (Geha et al. 2012). For present-day, red UDGs in groups/clusters, there is evidence that suggests they formed as (physically large) blue LSB dwarf galaxies in the field and were transformed during their infall onto dense environments (Román & Trujillo 2017b). Motivated by these previously observed trends, we start by presenting the colors of our sample and defining blue and red galaxies, which will be a useful point of comparison.

Intriguingly, our LSBG sample shows evidence for color bimodality in both $g - r$ and $g - i$, with a clear correlation between color and galaxy morphology. In Figure 3, we show our sample in the color–color diagram $g - r$ versus $g - i$. We separate red and blue galaxies using the median $g - i$ color (dashed black line): red galaxies are defined to have $g - i \geq 0.64$, and blue galaxies are defined to have $g - i < 0.64$. We note that

Table 1
Low Surface Brightness Galaxy Catalog Description

Column Name	Unit	Description
id		Unique LSBG id
R.A.	deg	Right ascension (J2000)
Decl.	deg	Declination (J2000)
$\mu_0(i)$	mag arcsec $^{-2}$	i -band central surface brightness
$\sigma(\mu_0(i))$	mag arcsec $^{-2}$	Uncertainty of $\mu_0(i)$
m_i	mag	i -band apparent magnitude
$\sigma(m_i)$	mag	Uncertainty of m_i
$g - r$	mag	$g - r$ color
$g - i$	mag	$g - i$ color
r_{eff}	arcsec	Effective radius
$\sigma(r_{\text{eff}})$	arcsec	Uncertainty of r_{eff}
n		Sérsic index
$\sigma(n)$		Uncertainty of n
ϵ		Ellipticity
$\sigma(\epsilon)$		Uncertainty of ϵ
A_g	mag	g -band Galactic extinction
A_r	mag	r -band Galactic extinction
A_i	mag	i -band Galactic extinction

Note. Magnitudes are on the AB system and have not been corrected for Galactic extinction. We provide Galactic extinction corrections, which are derived from the Schlafly & Finkbeiner (2011) recalibration of the Schlegel et al. (1998) dust maps.

(This table is available in its entirety in machine-readable form.)

Table 2
Archival *GALEX* Measurements

Column Name	Unit	Description
id		Unique LSBG id
R.A.	deg	Right Ascension (J2000)
Decl.	deg	Declination (J2000)
NUV	mag	Near-UV apparent magnitude
$\sigma(\text{NUV})$	mag	Uncertainty of NUV
FUV	mag	Far-UV apparent magnitude
$\sigma(\text{FUV})$	mag	Uncertainty of FUV
Survey		<i>GALEX</i> survey name

Note. Magnitudes are on the AB system and have not been corrected for Galactic extinction. The coordinates are those of the matched source in the *GALEX* source catalog (see Section 5.1.4).

(This table is available in its entirety in machine-readable form.)

modeling the $g - i$ color distribution as a sum of two Gaussians yields a color boundary within 0.01 mag of the median; we choose to use the median for simplicity. Evidence for color bimodality can be seen in the associated histograms on the top and right side of the figure. As an additional test of the apparent bimodality, we performed kernel density estimation on both distributions, assuming Gaussian kernels with bandwidths determined by a cross-validation grid search over a reasonable range of widths. The results are shown as black lines overlaid on each histogram; we see that the bimodality in both color distributions appears to be robust to our choice of density estimation method.

Our sample’s median $g - i$ color of 0.64 is consistent with UDG candidates around Abell Cluster 168 and its surrounding large-scale structure (Román & Trujillo 2017a); this galaxy

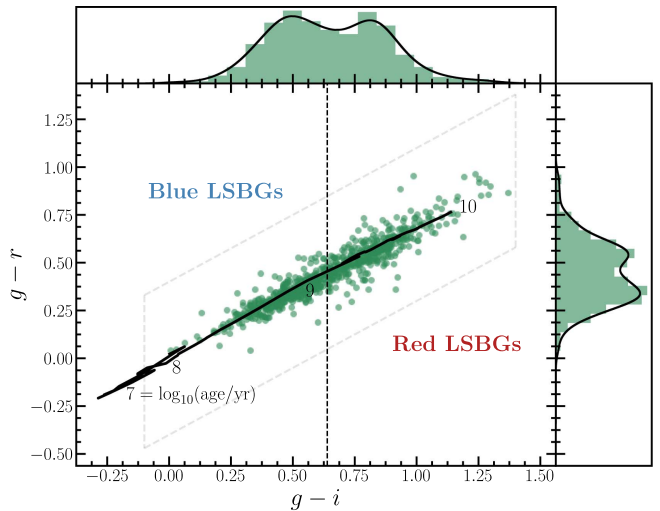


Figure 3. Color–color diagram for our full catalog of LSBGs. We separate the galaxies into red ($g - i \geq 0.64$) and blue ($g - i < 0.64$) subsamples, with the dividing color at the median value. We show the evolutionary path of a $0.4 \times$ solar metallicity simple stellar population from the models of Bruzual & Charlot (2003). The subsolar and solar metallicity models fall on very similar evolutionary paths in this color space. The black lines overlaid on the histograms on the top and right side of the figure show the density distributions obtained from kernel density estimation using a Gaussian kernel. The dashed gray box shows our color selection region (Section 3.3).

sample is composed of blue and red LSBGs with median $g - i = 0.66$. The red LSBGs in our sample have median $g - i = 0.8$, which is similar to the population of UDGs in the Coma Cluster (van Dokkum et al. 2015). In contrast, our blue LSBGs are much bluer with median $g - i = 0.47$, which is comparable to the average $g - i$ color of 0.45 observed in a sample of H I-rich UDGs in the field (Leisman et al. 2017).

In Figure 3, we also show the evolutionary path of a $0.4 \times$ solar metallicity stellar population from the models of Bruzual & Charlot (2003). The subsolar and solar metallicity models follow very similar tracks in this color space, so we cannot set meaningful metallicity constraints with the available colors. The red LSBGs are consistent with being composed of mostly old stars, whereas the colors of the blue LSBGs require young stellar populations.

In addition to their difference in color, the red and blue galaxies have visibly distinct morphologies. In Figure 4, we show gri -composite images of representative galaxies from each subsample, spanning the distribution of surface brightnesses and sizes. The blue galaxies tend to have irregular, lumpy morphologies and compact star formation regions. In addition, most (76%) of the blue sources have ultraviolet (UV) detections in the *GALEX* source catalog (see Section 5.1.4), suggesting ongoing star formation in these systems. In contrast, the red galaxies typically have spherical or elliptical shapes with light profiles that are well characterized by single-component Sérsic functions. The observed properties of these galaxies are consistent with early-type dwarf galaxies, and some fraction may be physically similar to UDGs in dense galaxy clusters, depending on their (unknown) distances.

In the following sections, we present and compare properties of the red and blue subsamples following the above $g - i$ color definition.

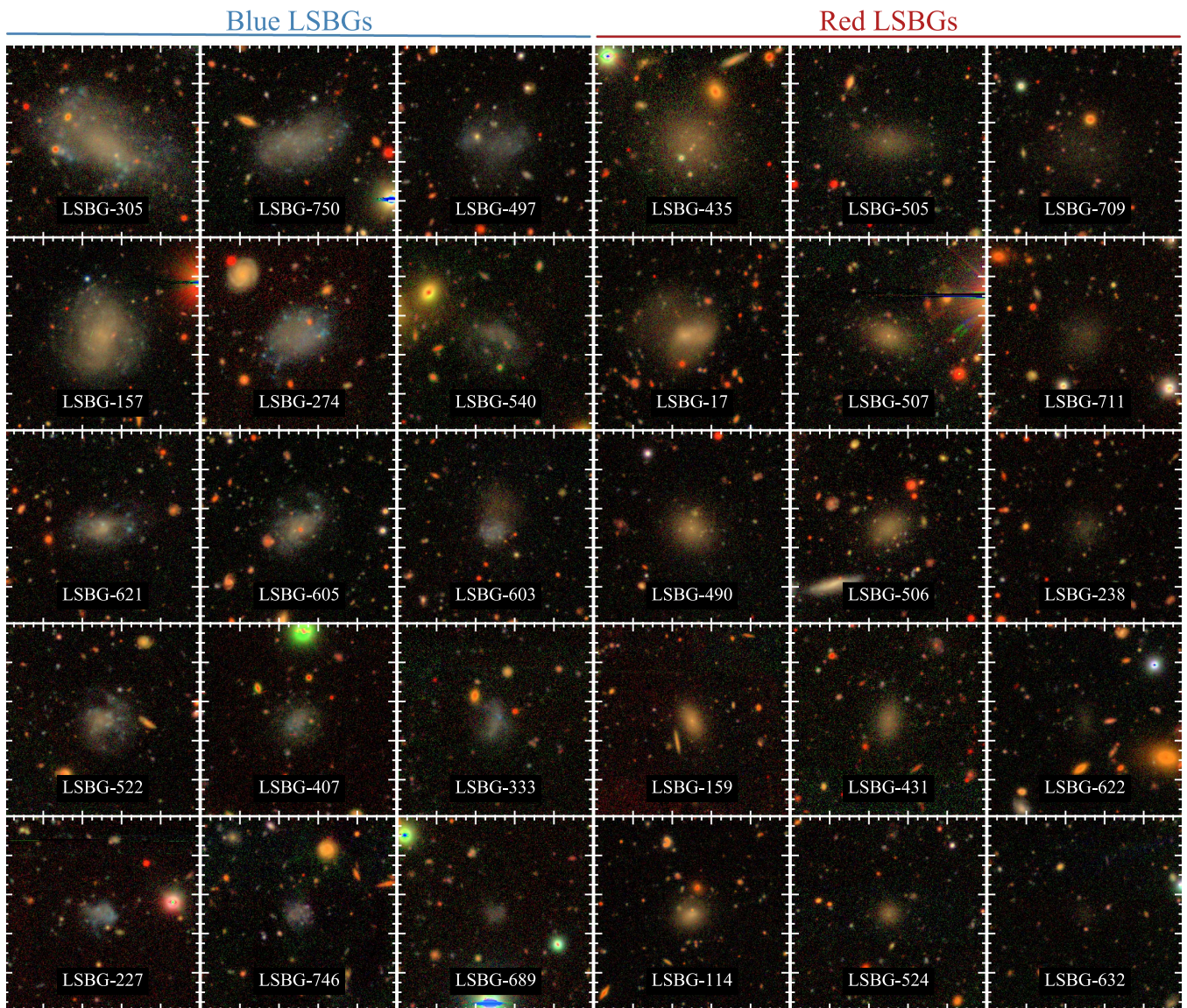


Figure 4. HSC-SSP *gri*-composite images (Lupton et al. 2004) of representative blue (left; $g - i < 0.64$) and red (right; $g - i \geq 0.64$) galaxies from our LSBG sample. Each cutout is $55''$ on a side. For each subsample, size (surface brightness) roughly decreases from top to bottom (left to right). The blue galaxies are generally irregular systems, whereas the red galaxies tend to be elliptical.

4.2. Spatial Distribution

In Figure 5, we show the sky positions of LSBGs in our sample (colored points) within each HSC-SSP field. Following the above definition, red LSBGs are shown as red points and blue LSBGs as blue points. Our selection on large size ($r_{\text{eff}} > 2.5''$) likely restricts most of our sample to low redshift. For reference, we plot the positions of low- z galaxies with known redshifts from the NASA-Sloan Atlas¹⁴ (NSA), which contains virtually all galaxies with known redshifts out to $z = 0.055$ within the coverage of SDSS Data Release 8 (DR8; Aihara et al. 2011). The overlap between the NSA and HSC-SSP is not perfect, so regions with few black points (e.g., the northern region in the bottom right panel) are not necessarily representative of the associated low- z galaxy population.

Without spectroscopic redshifts for a large fraction of the objects in our sample, a cross-correlation analysis (e.g., Ménard

et al. 2013) may be used to estimate the redshift distribution and statistically infer the physical nature of these objects. We leave such an analysis for future work. Interestingly, however, we can already see that sources in our sample are not distributed uniformly on the sky—many cluster both with other LSBGs and with higher surface brightness low- z galaxies, and the effect appears to be stronger for the red LSBGs (see Section 5.2 for a detailed look at one of these overdensities). However, it is important to emphasize that detailed auto- and cross-correlation analyses are necessary to make robust claims about the clustering of these objects.

4.3. Surface Brightness and Shape Distributions

We now turn to the distributions of the best-fit Sérsic parameters. In the left panel of Figure 6, we compare the relationship between effective radius r_{eff} (measured along the major axis) and mean surface brightness $\bar{\mu}_{\text{eff}}(g)$ (measured within the *circularized* effective radius) for the red and blue

¹⁴ <http://nsatlas.org>

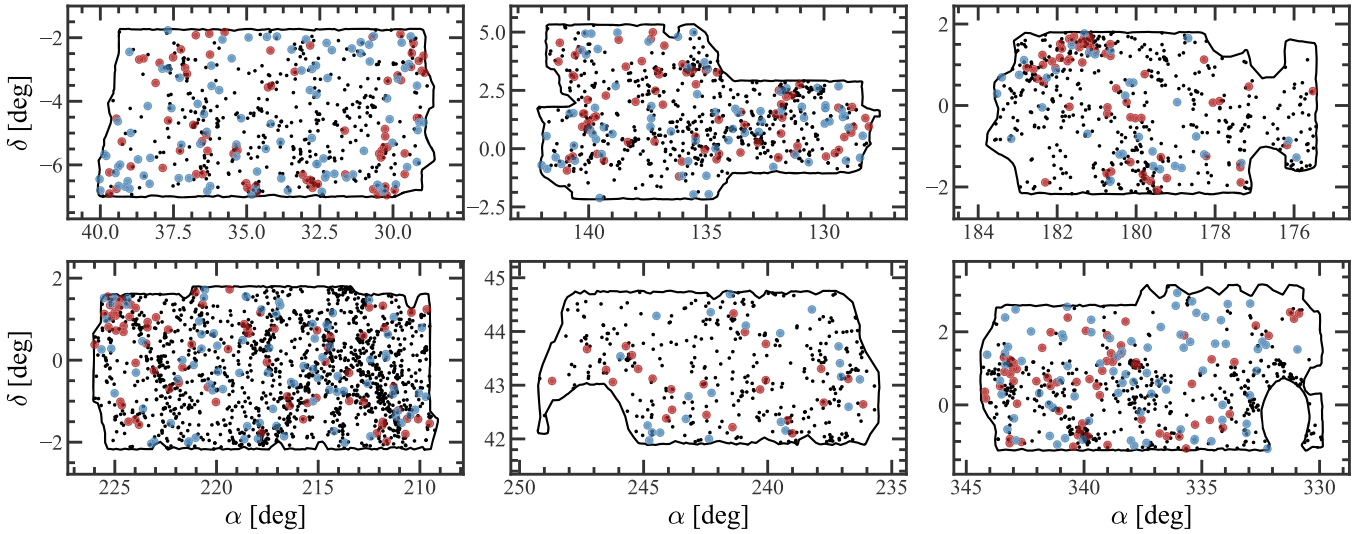


Figure 5. Sky positions of LSBGs within the six HSC-SSP fields that have been observed to the full Wide layer depth (in *gri*) as of the internal S16A data release (see Aihara et al. 2018b for information about the HSC-SSP data releases). Red LSBGs ($g - i \geq 0.64$) are colored red, and blue LSBGs ($g - i < 0.64$) are colored blue. We also show the positions of galaxies with $z < 0.055$ (black points) from the NSA galaxy catalog.

subsamples. The radius distributions are very similar—both span a wide range of $r_{\text{eff}} \sim 2''.5\text{--}14''$ and have a median value of $\sim 4''$. In contrast, the mean surface brightness distributions are dramatically different. The red distribution is much broader with 16th, 50th, and 84th percentiles of $\bar{\mu}_{\text{eff}}(g) = 24.8, 25.8$, and $26.8 \text{ mag arcsec}^{-2}$, respectively. For the blue galaxies, the same percentiles are $\bar{\mu}_{\text{eff}}(g) = 24.5, 24.8$, and $25.5 \text{ mag arcsec}^{-2}$. Hence, the blue LSBGs typically have higher mean surface brightnesses than the red LSBGs. In addition, galaxies that are both faint ($\bar{\mu}_{\text{eff}}(g) > 26 \text{ mag arcsec}^{-2}$) and large in angular extent ($r_{\text{eff}} > 6''$) are almost exclusively red. The black dashed line shows our selection cut at $\bar{\mu}_{\text{eff}}(g) = 24.3 \text{ mag arcsec}^{-2}$.

In the right panel of Figure 6, we show Sérsic index n versus central surface brightness $\mu_0(g)$. In general, the blue LSBGs have brighter central surface brightnesses than the red LSBGs, with median values of $\mu_0(g) = 24.0 \text{ mag arcsec}^{-2}$ and $\mu_0(g) = 24.9 \text{ mag arcsec}^{-2}$, respectively. The red distribution is again the broader of the two: 79 red galaxies have $\mu_0(g) > 26 \text{ mag arcsec}^{-2}$, whereas only 11 blue galaxies reach such low central surface brightnesses. Again, the black dashed line represents our cut on $\bar{\mu}_{\text{eff}}(g)$, which produces a curve in the $\mu_0\text{--}n$ plane. The horizontal histogram in the right panel of Figure 6 compares the red and blue Sérsic index distributions. For comparison, the black line shows the same distribution for a sample of 753 UDGs in the Coma Cluster (Yagi et al. 2016). All three distributions favor nearly exponential light profiles, with a median index of $n \sim 0.9$.

We show ellipticity distributions in Figure 7. The LSBGs are generally round, with a median $\epsilon = 0.3$ for the full sample. While our selection removes sources with $\epsilon > 0.7$, the distribution begins to fall before this threshold, particularly for the blue galaxies. The dashed black line shows the distribution for UDGs in Coma, which are also overwhelmingly round systems. For randomly oriented disks, the expected ellipticity distribution is much flatter between $\epsilon = 0.1$ and 0.7 . This can be seen in the green line, which shows the distribution for a sample of spiral galaxies from SDSS (Rodríguez & Padilla 2013) that were classified by the Galaxy Zoo project (Lintott et al. 2008).

4.4. High- μ_0 Sources

Both the red and blue $\mu_0(g)$ distributions have an HSB tail, composing a very small fraction of the sample. Less than 5% of our sample has $\mu_0(g) < 22 \text{ mag arcsec}^{-2}$. This is due to our selection on $\bar{\mu}_{\text{eff}}(g)$ rather than $\mu_0(g)$. As described in Section 3.4, we cut on mean surface brightness to allow nucleated sources into our sample. Consistent with our selection, high central surface brightnesses are associated with high n values, which are indicative of compact, relatively bright cores. In most cases ($\sim 50\%$ of high- μ_0 sources), these cores are bright bulge-like components embedded in an LSB disk, similar to what is seen in the population of giant LSB spirals (e.g., Sprayberry et al. 1995), of which Malin 1 (Bothun et al. 1987) represents the most extreme example. In the other cases, there is a bright central star formation region or potential nuclear cluster that drives the fit toward high- n /high- μ_0 values.

In the top row of Figure 8, we show *gri*-composite images of example high- μ_0 sources. From left to right, the central surface brightness is high owing to a central star formation region, a bulge within an LSB spiral, a bulge-like core within a smooth red spheroid (in projection), and an apparent central point source (nuclear cluster). The bottom row of this figure shows the surface brightness profile of each galaxy extracted within elliptical apertures using the shape parameters from *imfit* (Section 3.4). We also show profiles extracted using the same apertures on two-dimensional model images, where each galaxy is modeled as a PSF-convolved Sérsic function with the best-fit parameters from *imfit*. The central surface brightnesses—which, in our catalog, are based on the deconvolved Sérsic model—are higher than traditional definitions of LSBGs (optical μ_0 fainter than $\sim 22\text{--}23 \text{ mag arcsec}^{-2}$). However, these sources are LSB on average, and their relation to non-nucleated/bulgy LSBGs deserves further investigation. We therefore include them in our catalog, noting that they represent a small fraction of our sample.

5. Source Cross-matching

Given the LSB nature of our catalog, few sources have previous redshift measurements, and most archival photometric

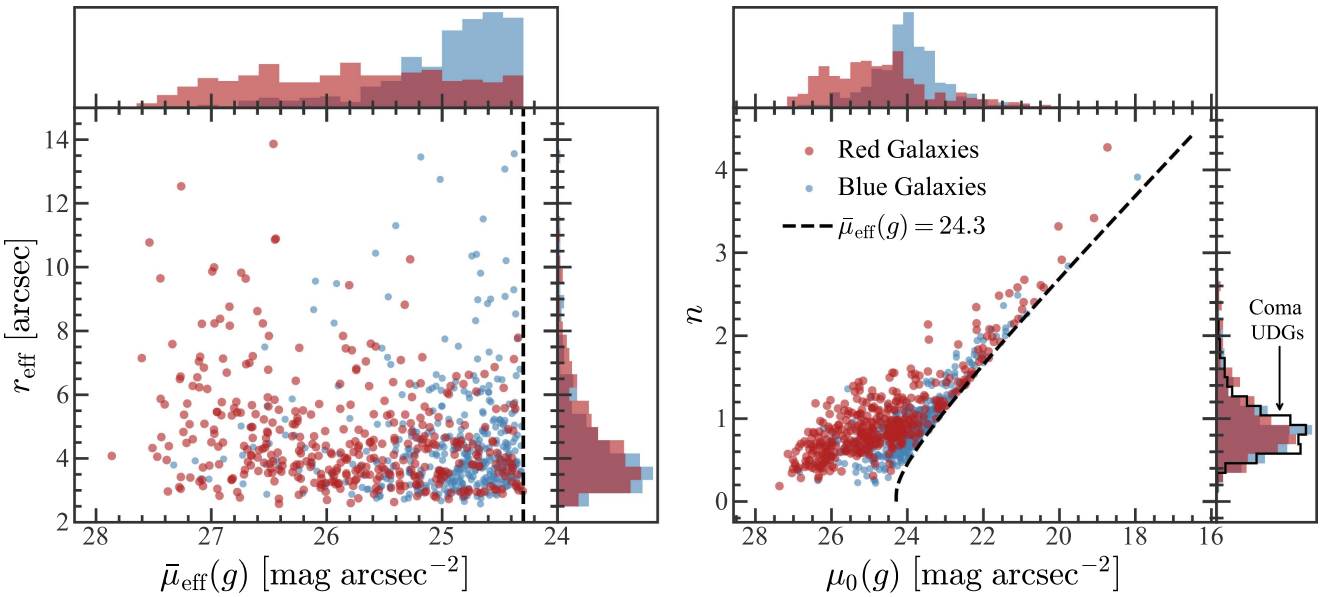


Figure 6. Left: relationship between effective radius r_{eff} and g -band mean surface brightness within the circularized effective radius $\bar{\mu}_{\text{eff}}(g)$ for our LSBG sample. The independent parameter distributions are shown as histograms on the top and right side of the figure. Points and histograms are colored according to the galaxy color definition described in Section 4.1. Right: Sérsic index n vs. g -band central surface brightness $\mu_0(g)$ for the same galaxy samples shown in the left panel. Since we select galaxies based on $\bar{\mu}_{\text{eff}}(g)$, there is an HSB tail associated with high Sérsic n values. These high- n (and thus high- μ_0) galaxies, which make up less than 5% of our sample, generally have bright cores or central star-forming regions. For comparison, we show the Sérsic n distribution of UDGs in the Coma Cluster (Yagi et al. 2016) as the black line in the horizontal histogram on the right. In both panels, the dashed black line shows our selection cut at $\bar{\mu}_{\text{eff}}(g) = 24.3$ mag arcsec $^{-2}$, which results in a curve in the $\mu_0 - n$ plane.

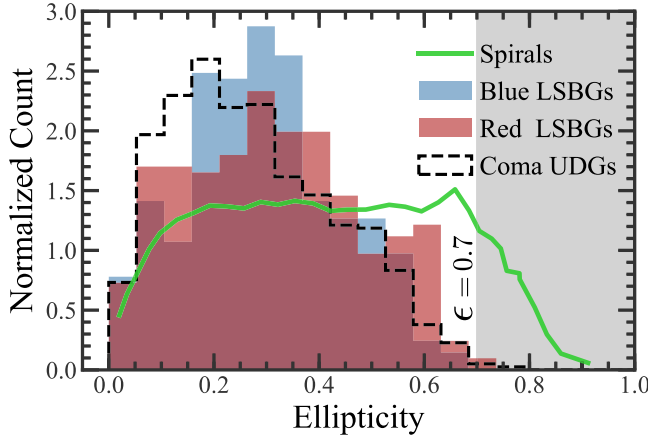


Figure 7. Ellipticity (ϵ) distributions of our red and blue LSBG subsamples, UDGs in the Coma Cluster (Yagi et al. 2016), and spiral galaxies from SDSS (Rodríguez & Padilla 2013) that were classified by the Galaxy Zoo project (Lintott et al. 2008). We select galaxies with $\epsilon < 0.7$; values outside this range are shaded gray.

data lack the depth needed to accurately characterize our sources. Nonetheless, it is still possible to gain insight into the physical properties spanned by galaxies in our sample by cross-matching with existing catalogs. Therefore, in this section, we present results from cross-matching with archival data ranging from radio to UV wavelengths. We show LSBGs with distance information in the size–luminosity plane in Section 5.4.

5.1. External Wide-field Surveys

5.1.1. SDSS Photometric Catalog

While the vast majority of sources in our sample have surface brightnesses near or below the detection limit of SDSS (e.g., Blanton et al. 2005), many still have detections in the

SDSS photometric catalog. In Figure 9, we show the distribution of $\bar{\mu}_{\text{eff}}(g)$ (as we measured with HSC-SSP) for galaxies with a matched source in SDSS DR12, where we consider objects within $3''$ a match. The SDSS detections drop quickly to zero for surface brightnesses fainter than 25.5 mag arcsec $^{-2}$, and as the red histogram shows, more than half of our red LSBGs exist within this region of parameter space. At these surface brightnesses, it is important to note that a detection in the SDSS photometric catalog does not necessarily mean that the photometry is reliable. For example, if the center of an LSBG is detected, its outer profile may fall below the detection limit, resulting in its size and magnitude being underestimated by the SDSS photometric pipeline. See the middle row of Figure 10 for example SDSS gri -composite images of some of our largest LSBGs.

5.1.2. The NASA-Sloan Atlas

Redshifts are crucial for interpreting the physical nature of individual galaxies. Unfortunately, our LSBGs are generally too faint to be in the SDSS spectroscopic catalog (two exceptions are given below). To search for LSBGs with previous (optical) spectroscopic redshifts, we cross-match with the NSA galaxy sample, which was selected to include virtually all known redshifts out to $z = 0.055$ within the coverage of SDSS DR8. We find three matches that are within $2''$ from objects in our sample.

Two of the matches are physically large, face-on LSB spirals from the SDSS spectroscopic catalog: LSBG-171 (NSA ID 42601) and LSBG-456 (NSA ID 145288). LSBG-171 is at $z = 0.04389$ and has $r_{\text{eff}} = 6.7$ kpc and $\mu_0(g) = 22.1$ mag arcsec $^{-2}$ (we correct for cosmological dimming when redshift information is available). LSBG-456 is at $z = 0.02863$ and has $r_{\text{eff}} = 5.9$ kpc and $\mu_0(g) = 23.8$ mag arcsec $^{-2}$, similar in size and central surface brightness to UDGs, although its absolute magnitude of $M_g = -17.9$ is nearly 3

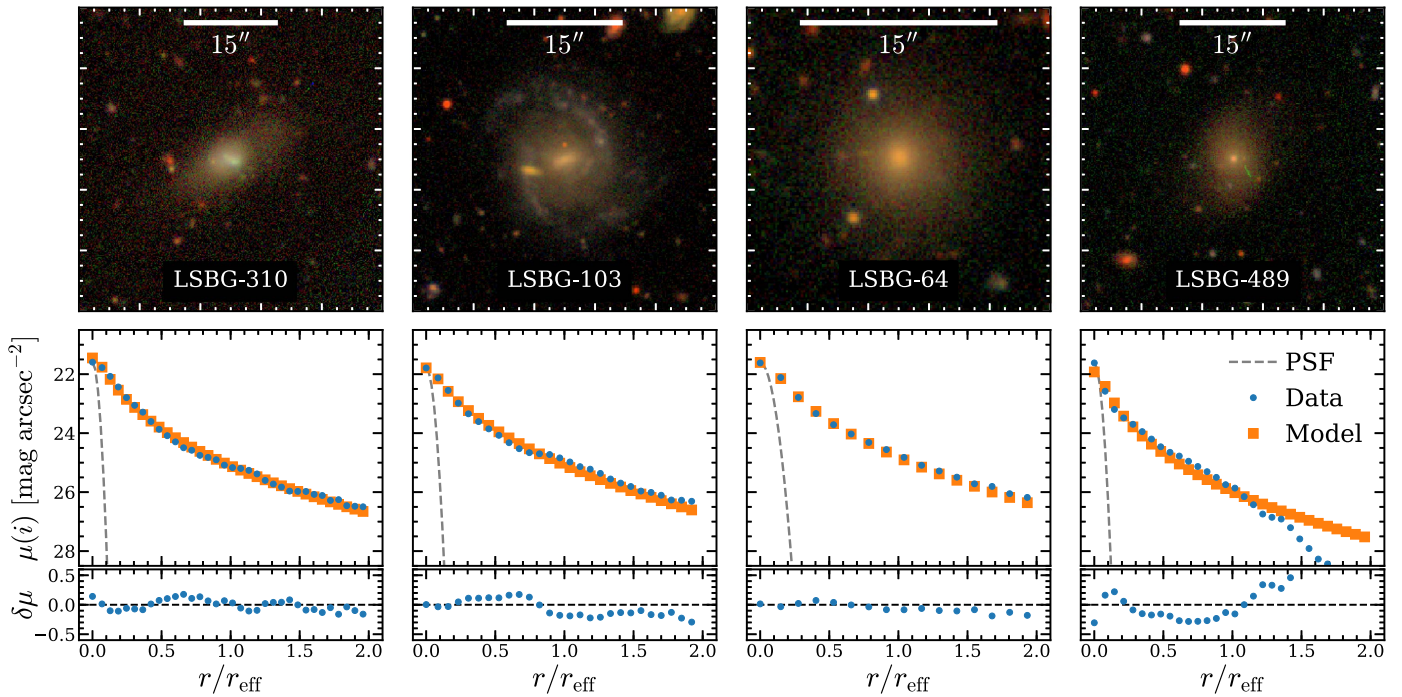


Figure 8. Top: example *gri*-composite HSC-SSP images of high- μ_0 (and thus high- n) sources, which represent $<5\%$ of our sample (see right panel of Figure 6). From left to right, we show galaxies whose central surface brightness is high owing to a central star-forming region, an apparent bulge within an LSB disk, a bulge-like core in a red spheroidal galaxy, and an apparent point source (nuclear cluster). The angular scale is indicated by the white bar at the top of each panel. Bottom: radial *i*-band surface brightness profiles of each galaxy (blue circles), where we use elliptical apertures with shape parameters given by our two-dimensional Sérsic fits. For each galaxy, we scale the radial coordinate by the effective radius. For comparison, we show the angular scale of the PSF (gray dashed lines) and model profiles generated using the same apertures on two-dimensional, PSF-convolved Sérsic model images (orange squares). The lower panels show the residuals between the measured profiles and the Sérsic models.

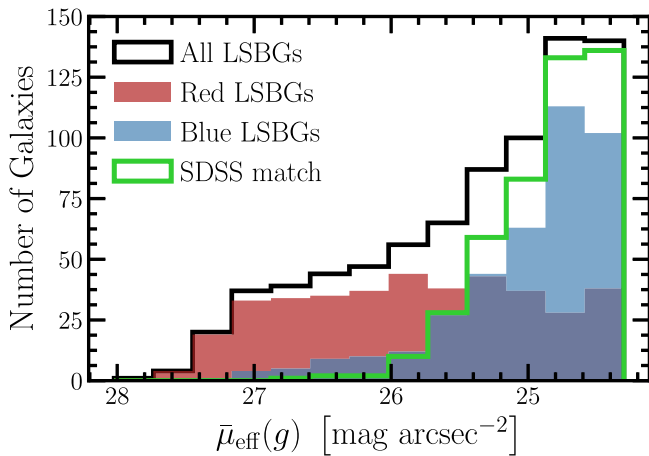


Figure 9. Distribution of mean surface brightness for LSBGs with a detection in the SDSS DR12 photometric catalog (green histogram), where we consider objects within $3''$ a match. We also show the distribution for our full galaxy sample (black histogram) and our blue (blue histogram) and red (red histogram) subsamples. Note that the SDSS detections are near the detection limit of the survey, making the photometry less reliable (see Figure 10 for SDSS images of LSBGs).

mag brighter than the most luminous UDGs discovered by van Dokkum et al. (2015).

The third match is LSBG-613 (NSA ID 144517). This LSBG has a redshift of $z = 0.02447$, which was measured during a survey for LSB dwarf galaxies (Roberts et al. 2004). Its inferred physical effective radius is $r_{\text{eff}} = 3.3$ kpc, and its central surface brightness is $\mu_0(g) = 23.9$ mag arcsec $^{-2}$, again putting it near the UDG size–surface brightness parameter space.

5.1.3. ALFALFA

The gas mass fractions of LSB dwarf galaxies are among the highest of any known galaxy type (as high as $f_{\text{gas}} = 0.95$; Schombert et al. 2001). Such gas-rich systems are probed by radio surveys tuned to measure the 21 cm line of atomic hydrogen (HI). The largest-volume blind HI survey to date is the Arecibo Legacy Fast Arecibo L-band Feed Array (ALFALFA; Giovanelli et al. 2005). We cross-match our sample with the 70% ALFALFA catalog¹⁵ (Haynes et al. 2011), which covers 70% of their final survey area; 361 of our LSBGs fall within this footprint.

The ALFALFA team visually inspected every HI source in their catalog and searched for optical counterparts using optical images from the Palomar Digital Sky Survey and, where available, the SDSS. We cross-match our sample with their assigned optical coordinates and find three matched sources. Given the higher image quality afforded by HSC-SSP, we also cross-match with ALFALFA’s full list of HI coordinates to cross-check their chosen optical counterparts. We consider any source with HI coordinates within 1.75 (approximately half of Arecibo’s beam) of an LSBG in our sample. This produced 17 matches with an ALFALFA detection code of 1 (12 sources) or 2 (5 sources), where code 1 refers to high signal-to-noise ratio HI detections with reliable optical counterparts, and code 2 refers to low signal-to-noise ratio HI detections with optical counterparts whose (optical) redshifts are consistent with the HI line measurements (Haynes et al. 2011). We then visually inspected each match. We recover the three optical matches

¹⁵ The ALFALFA 70% catalog is publicly available at <http://egg.astro.cornell.edu/alfalfa/data/index.php>.

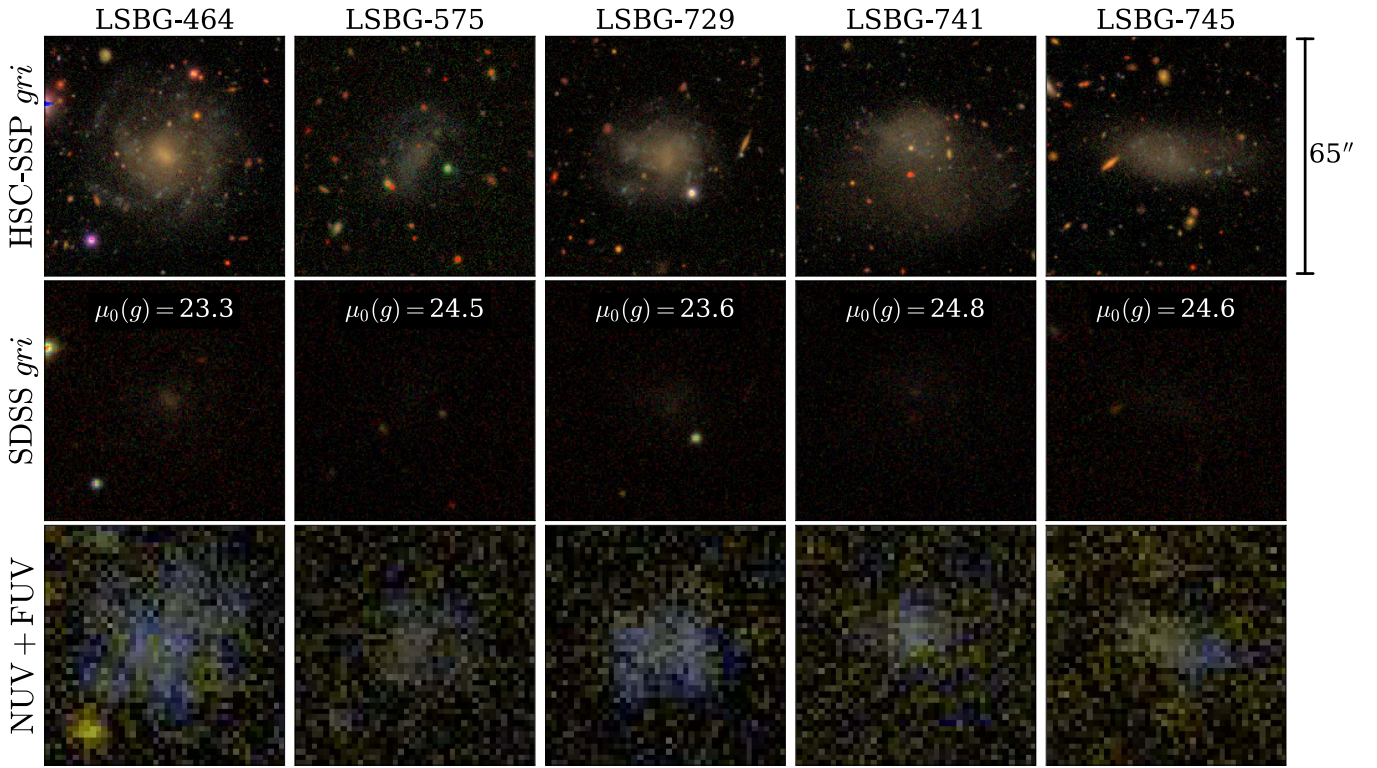


Figure 10. Cutout images from HSC-SSP (top row), SDSS (middle row), and *GALEX* (bottom row) showing some of the largest LSBGs in our sample. The *gri*-composite images from HSC-SSP and SDSS were created using the same stretch following the method of Lupton et al. (2004). Each cutout image is 65'' on a side. LSBG-464 ($z = 0.02573$) and LSBG-575 (distance = 29.5 Mpc) are in the 70% ALFALFA catalog (see Section 5.1.3), and LSBG-729 ($z = 0.02513$) hosted a Type IIb supernova in 2009 (see Section 5.3).

above, and in all other cases, the optical counterpart assigned by the ALFALFA team is a higher surface brightness galaxy. While we cannot rule out the possibility that any of our matched sources are also contributing to the observed H I signals, we assume that the ALFALFA-selected optical counterparts are correct. Hence, we have three LSBGs with an H I counterpart in the 70% ALFALFA catalog.

Two of the matches are physically large face-on LSB spirals, one of which was matched with the NSA above: LSBG-456 (NSA ID 145288 and AGC 243463) and LSBG-464 (AGC 249425). Similar to the NSA-matched galaxies, LSBG-464's redshift of $z = 0.02573$ implies that it is physically large, with an effective radius of $r_{\text{eff}} = 6.0$ kpc. Images of LSBG-464 from HSC-SSP, SDSS, and *GALEX* can be seen in the first column of Figure 10. While there is a clear detection of the galaxy's core in the SDSS image, the giant disk and spiral arms are only visible in the HSC-SSP image, highlighting the need for deep imaging in searches for LSBGs. The strong detection of the disk in the UV by *GALEX* reflects ongoing star formation throughout the disk.

The third match with ALFALFA is LSBG-575 (AGC 189086). We show images of this source from HSC-SSP, SDSS, and *GALEX* in the second column of Figure 10. This LSBG is relatively nearby at a distance of 29.5 Mpc, its H I mass is $\log_{10}(M_{\text{H I}}/M_{\odot}) = 8.08$, and it has a low velocity width (at 50% of the peak flux) of 26 km s⁻¹. For context, the mean width for all ALFALFA galaxies is 194 km s⁻¹ (Leisman et al. 2017). From HSC-SSP optical data, we find that LSBG-575 has a central surface brightness of $\mu_0(g) \sim 24.5$ mag arcsec⁻². Its irregular morphology makes size measurements highly uncertain; nevertheless, we estimate it to have a large effective radius

of $r_{\text{eff}} = 11''$, which at its distance corresponds to a physical size of $r_{\text{eff}} = 1.6$ kpc. These physical properties are consistent with LSBG-575 being a gas-rich UDG.

Assuming the mass-to-light ratio/color relation derived from Bell et al. (2003), LSBG-575 has a stellar mass of $M_{\star} \sim 2.6 \times 10^7 M_{\odot}$, implying an H I-to-stellar-mass ratio of $M_{\text{H I}}/M_{\star} = 4.7$, a factor of 7 lower than the mean value of the H I-bearing UDGs discovered by Leisman et al. (2017). Following Schombert et al. (2001), we use this ratio to estimate the baryonic gas fraction as

$$f_{\text{gas}} = \frac{M_{\text{gas}}}{M_{\text{gas}} + M_{\star}} \approx \left(1 + \frac{M_{\star}}{1.4 M_{\text{H I}}}\right)^{-1}, \quad (1)$$

where M_{gas} is the total gas mass, and the factor of 1.4 assumes a solar hydrogen mass fraction. For LSBG-575, we find a high gas fraction of $f_{\text{gas}} \approx 0.87$, which is not uncommon at this stellar mass (e.g., Geha et al. 2006; Kim 2007; Bradford et al. 2015).

In summary, LSBG-575 has a low H I mass compared to the ALFALFA population (but consistent with the expectation given its stellar mass) and a high gas fraction, which is typical for objects of its stellar mass but lower than other H I-bearing UDGs (e.g., Papastergis et al. 2017).

5.1.4. *GALEX*

A galaxy's integrated UV light, which is dominated by young, massive stars, is a well-known tracer of its current star formation rate (SFR). To get a sense for the fraction of objects in our sample with ongoing star formation, we cross-match with the *GALEX* source catalog (Martin et al. 2005) using the

MAST Portal.¹⁶ We adopt a separation threshold of 4'' (e.g., Budavári et al. 2009) for matched sources. Following the *GALEX* DR6 documentation, we drop matched sources with artifact flags associated with dichroic reflections (NUV_ARTIFACT = 4 or FUV_ARTIFACT = 4) and/or window reflections (NUV_ARTIFACT = 2; NUV detector only). In addition, we drop sources with negative near-UV (NUV) magnitudes. Since the MAST archive contains all *GALEX* observations, sources with repeated observations have multiple entries in the catalog. For each matched source, we keep the *GALEX* observation with the longest NUV+far-UV (FUV) exposure time. If multiple observations have the same exposure time, we keep the source with the smallest offset from the position of the matched LSBG in our catalog.

Most of the sources in our catalog (761 out of 781) fall within the footprint of at least one *GALEX* survey.¹⁷ Of these *GALEX*-observed LSBGs, 374 (~50%) have UV detections. Of these detections, 80% are blue LSBGs, and of all the blue LSBGs in our sample, 76% have a UV counterpart in *GALEX*. The red LSBGs with *GALEX* detections (78 in total) may be interesting objects for follow-up studies—about half have $i - i > 0.7$.

For convenience, we give the existing NUV and FUV magnitudes for all matched sources, as well as the *GALEX* survey from which the data were taken, in machine-readable format; see Tables 1 and 2 for a summary of the contents of the catalog. We simply adopt the *GALEX* catalog magnitudes; these are not matched aperture measurements. Note that the *GALEX* surveys (i.e., the All-Sky Imaging, Medium Imaging, Deep Imaging, and Nearby Galaxy Surveys, and the Guest Investigator Program) image the sky to different depths.

In Figure 10, we show cutout images from HSC-SSP, SDSS, and *GALEX* of some of the largest LSBGs in our sample that also have *GALEX* detections. We show the SDSS images to give the reader a context from which to view the HSC-SSP images, which push to much lower surface brightness levels than is commonly seen from wide-field surveys.

The LSBGs with known distances suggest that our sample spans a distance range of (at least) ~ 30 –100 Mpc. Assuming this distance range, we estimate the range of SFRs as (Kennicutt 1998)

$$\text{SFR} [M_{\odot} \text{ yr}^{-1}] = 1.4 \times 10^{-28} L_{\nu} [\text{erg s}^{-3} \text{ Hz}^{-1}], \quad (2)$$

where L_{ν} is the UV luminosity derived from the extinction-corrected FUV magnitudes. We estimate the Galactic reddening $E(B - V)$ using the maps of Schlegel et al. (1998) and the (Cardelli et al. 1989) extinction law with $R_V = A_V/E(B - V) = 3.1$ and $A_{\text{FUV}} = 8.24 E(B - V)$ (Wyder et al. 2007); we do not account for internal dust extinction. For the assumed distance range, the median SFR of our sample (including only objects with FUV measurements) spans a range of ~ 0.002 – $0.02 M_{\odot} \text{ yr}^{-1}$, where these values are likely lower limits, since we have ignored internal dust extinction. Assuming the mass-to-light ratio/color relation derived from Bell et al. (2003), this same distance range implies a median stellar-mass range of $M_{\star} \sim 10^7$ – $10^8 M_{\odot}$. With such parameters,

these objects are consistent with the observed SFR– M_{\star} relation for H I-selected galaxies from the ALFALFA survey (Huang et al. 2012; Leisman et al. 2017).

5.2. Early-type Dwarfs in a Nearby Galaxy Group

As noted in Section 4.2, many of the red LSBGs appear to cluster with one another, as well as with higher surface brightness low- z galaxies. This clustering can be used to statistically estimate the distances to an ensemble of sources (e.g., van der Burg et al. 2016). Here, we highlight one of the largest overdensities of LSBGs, which can be seen in the bottom left panel of Figure 5 near $(\alpha, \delta) = (225^{\circ}, +1^{\circ})$.

Within this region, there are at least 27 LSBGs (19 red and 8 blue) clustered within 1.5 times the projected second turnaround radius (Bertschinger 1985) of the NGC 5846 galaxy group, a nearby group at 26.1 Mpc (Tonry et al. 2001). With a virial mass of $\sim 8 \times 10^{13} M_{\odot}$ (Mahdavi et al. 2005), this group is the third most massive collection of early-type galaxies in the local universe after the Virgo and Fornax Clusters, and it has been studied extensively at many different wavelengths (e.g., Tully 1987; Mulchaey et al. 2003; Eigenthaler & Zeilinger 2010; Machacek et al. 2011; Marino et al. 2016). In the bottom panel of Figure 11, we show the sky positions of potential group members (black points) from a study of the galaxy population down to luminosities as faint as $M_R = -10$ (Mahdavi et al. 2005). Galaxies within this group are predominantly of early type, and the system is dominated by the giant ellipticals NGC 5846 and NGC 5813 (green stars). The large circle shows the boundary of the second turnaround radius (0.84 Mpc) at the distance to the group. The white region in the bottom right corner of the figure shows the coverage of the HSC-SSP, which only overlaps with a small fraction of the group.

The open red (blue) circles in Figure 11 show red (blue) LSBGs from this work. Sources also detected by Mahdavi et al. (2005) have a black point within the open circle. As the figure shows, there is considerable overlap between our catalogs. The Mahdavi et al. (2005) sources within the HSC-SSP footprint that are not in our catalog generally have much higher surface brightness than our objects of interest; a couple were within the halo of a bright star and were masked by our bright-object mask. Mahdavi et al. (2005) detect 14 sources from our sample that overlapped with their survey, most of which they assign as “possible” members.¹⁸ However, this is a statistical statement and does not apply to any specific object, since none from our sample have been confirmed as members via spectroscopic redshifts. At the distance of the NGC 5846 group, our LSBGs would have effective radii ranging from $r_{\text{eff}} \sim 0.5$ to 1.6 kpc and absolute magnitudes ranging from $M_g \sim -10.1$ to -13.4 mag, consistent with dwarf elliptical galaxies.

The NGC 5846 group is remarkably isolated in space. In the top panel of Figure 11, we show the redshift distribution of galaxies from the NSA catalog within 4° (1.8 Mpc) of the group center. There is a clear void between $z \sim 0.01$ and 0.02, which is in stark contrast to the background Hercules supercluster between $z \sim 0.03$ and 0.05. Any LSBGs that lie within this larger overdensity will have much more extreme

¹⁶ <https://mast.stsci.edu/>

¹⁷ To determine which sources were covered by any *GALEX* pointing, we cross-matched our LSBG catalog with the centers of all individual *GALEX* visits and checked whether the positions fell within the field-of-view radius from the center of any observation, as suggested by Bianchi et al. (2017).

¹⁸ This corresponds to a score of 2 on a 0–4 system, with 0 being a spectroscopically confirmed member and 4 being likely not a member. See Trentham et al. (2001) for details about how membership probabilities were assigned.

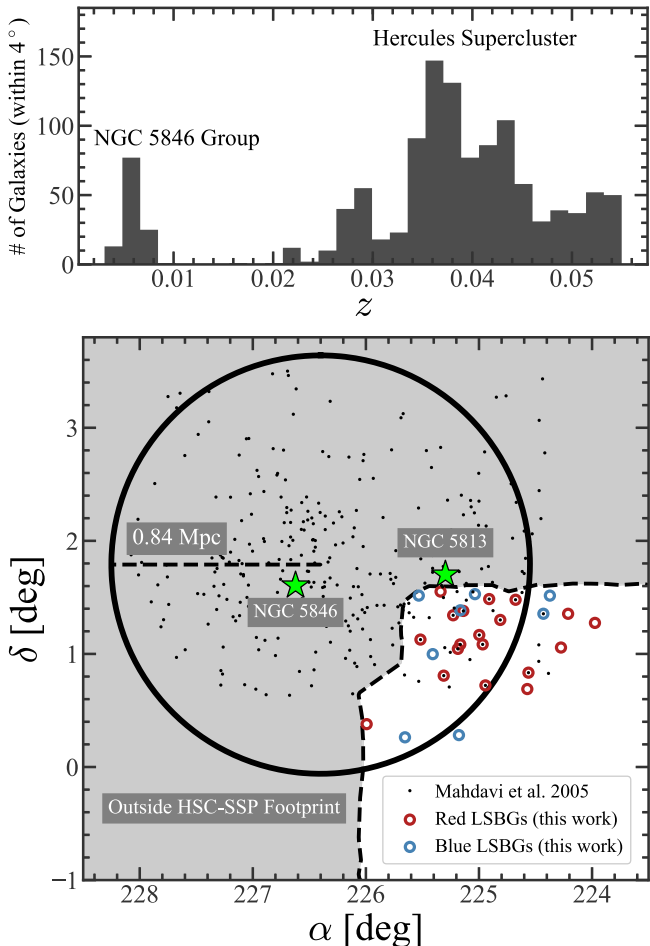


Figure 11. Top: redshift distribution from the NSA catalog of all galaxies with known redshifts (with $z < 0.055$) within 4° (1.8 Mpc) of the NGC 5846 group, which is remarkably isolated in space. The Hercules supercluster is behind this group and may host some of the LSBGs. Bottom: sky positions of potential NGC 5846 group members (black points) with luminosities as faint as $M_R = -10$ (Mahdavi et al. 2005). The group is dominated by the giant ellipticals NGC 5846 and NGC 5813 (green stars). The white region in the bottom right corner shows the HSC-SSP coverage near this group, and the open red (blue) circles show red (blue) LSBGs from this work. Sources also detected by Mahdavi et al. (2005) have a black point within the open circle. The large black circle shows the boundary of the second turnaround radius at the distance of the group.

physical properties. We note that many of the LSBGs in Figure 11 fall within the projected virial radii of multiple catalogued galaxy groups at $z \sim 0.04$ with halo masses in the range $\log_{10}(M_{\text{halo}}/M_{\odot}) \sim 12.5\text{--}13.0$ (Yang et al. 2007).

5.3. An LSB Supernova Host

Novae and supernovae have been called “beacons in the dark,” which can be used to detect LSBGs in the local universe (Conroy & Bullock 2015). A galaxy in our sample, LSBG-729, is a proof of concept for this idea. We show cutout images of LSBG-729 from HSC-SSP, SDSS, and GALEX in the third column of Figure 10. This galaxy hosted the Type I Ib supernova SN 2009Z (Zinn et al. 2012), which was discovered by the Lick Observatory Supernova Search (Filippenko et al. 2001) and classified by Stritzinger & Morrell (2009). Zinn et al. (2012) used SN 2009Z and LSBG-729 (called N271 in their work) to demonstrate that it is possible to discover LSBGs via the observation of ostensibly hostless supernovae. These authors

used archival optical imaging from SDSS and the 3.6 m New Technology Telescope to confirm the existence of this LSB host. They then obtained an H I spectrum of LSBG-729 using the 100 m Effelsberg Radio Telescope, confirming that it is at a similar redshift to SN 2009Z ($z = 0.02513$), and estimating an H I mass of $M_{\text{H}_1} = 2.96 \times 10^9 M_{\odot}$.

As can be seen in Figure 10, LSBG-729 also has a strong GALEX detection. Using Equation (2), we find an $\text{SFR} = 0.09 M_{\odot} \text{ yr}^{-1}$. Zinn et al. (2012) use SED fitting to estimate that extinction from the galaxy itself may be as high as $A_{\text{FUV}} \approx 2.5$. Accounting for this correction, we find a relatively high SFR of $0.9 M_{\odot} \text{ yr}^{-1}$, comparable to the Milky Way. Our estimates are about a factor of 2 larger than those of Zinn et al. (2012), which may be attributed to deeper UV data (we use data from GALEX’s Medium Imaging Survey, whereas they use the All-Sky Imaging Survey).

The HSC-SSP optical imaging is much deeper than was available to Zinn et al. (2012) (20-minute exposures on an 8.2 m mirror compared to 1- and 5-minute exposures on 2.5 and 3.5 m mirrors, respectively). This is particularly evident in Figure 10, where the HSC-SSP image of LSBG-729 reveals spiral structure and compact regions of star formation, whereas only its central region is marginally visible in the SDSS image. Using extinction-corrected HSC-SSP photometry and the same mass-to-light ratio/color relation as above, we estimate a stellar mass of $M_{\star} \approx 10^9 M_{\odot}$. Using Equation (1), this implies a gas fraction of $f_{\text{gas}} \approx 0.8$. This fraction is lower than the estimate of Zinn et al. (2012), which can be attributed to our larger stellar-mass estimate. At $z = 0.02513$, LSBG-729 has a large effective radius of ~ 4.6 kpc.

5.4. Size–Luminosity Relation

To summarize the distance information uncovered above: six LSBGs in our sample have archival spectroscopic redshifts (LSBG-171, LSBG-456, LSBG-464, LSBG-575, LSBG-613, and LSBG-729), and 27 LSBGs are projected in close proximity to a nearby galaxy group at 26.1 Mpc, which we will assume as their distance. Figure 12 shows the size–luminosity relation for these LSBGs. For context, we also show the family of early-type galaxies (Brodie et al. 2011), representative giant LSB spiral galaxies (Sprayberry et al. 1995), UDGs in intermediate- to high-density environments (van Dokkum et al. 2015; Román & Trujillo 2017a), and H I-bearing UDGs in the field (Leisman et al. 2017). We convert gr measurements to V band using the transformation $V = g - 0.59(g - r) - 0.01$ (Jester et al. 2005). For the UDGs, we assume $g - r = 0.47$, which is the mean color observed by Román & Trujillo (2017a). Galaxy sizes are represented by the circularized effective radius $r_{\text{circ}} = (1 - \epsilon)^{1/2} r_{\text{eff}}$ (note that the Leisman et al. [2017] objects were measured within circular apertures owing to low signal-to-noise ratio data).

Assuming that the 27 LSBGs (large triangles in Figure 12) are at the same distance as the NGC 5846 group, they are physically similar to dwarf spheroidals (dSphs) and dwarf ellipticals (dEs), with sizes ranging from $r_{\text{circ}} = 0.3$ to 1.2 kpc ($r_{\text{eff}} = 0.3$ to 1.6 kpc) and a median absolute magnitude of $M_V = -12$. If some of these LSBGs are in fact associated with the large overdensity behind this group (see Figure 11), then their sizes and luminosities could potentially be much larger.

The six LSBGs with previous redshift measurements (stars in Figure 12) span a wide range in size–luminosity parameter

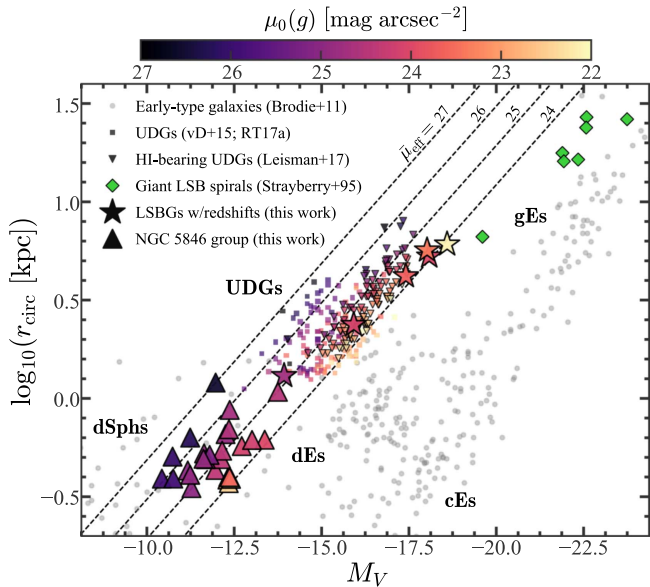


Figure 12. Size–luminosity relation for LSBGs in our sample for which we have distance information. Stars show LSBGs with archival spectroscopic redshifts, and large triangles show LSBGs that are projected in close proximity to the NGC 5846 group (see Figure 11), which is at a distance of 26.1 Mpc (we assume this distance for these LSBGs). We also show the family of early-type galaxies (Brodie et al. 2011), giant LSB spiral galaxies (Sprayberry et al. 1995), UDGs from van Dokkum et al. (2015) (vD+15) and Román & Trujillo (2017a) (RT17a), and H I-bearing UDGs (Leisman et al. 2017). The color bar shows the g -band central surface brightness for LSBGs in our sample and UDGs. The y -axis shows the logarithm of the circularized effective radius $r_{\text{circ}} = (1 - e)^{1/2} r_{\text{eff}}$. Lines of constant mean surface brightness are shown as dashed black lines.

space—from small UDGs with $r_{\text{circ}} = 1.3$ kpc ($r_{\text{eff}} = 1.6$ kpc) and $M_V = -14$ to giant LSB spirals with $r_{\text{circ}} = 6.1$ kpc ($r_{\text{eff}} = 6.7$ kpc) and $M_V = -19$. The largest/brightest of these objects occupy the region of parameter space that falls between UDGs and giant ellipticals, similar to the lower-luminosity end of previously known giant LSB spiral galaxies. As indicated by the color bar in Figure 12, these large sources are among the higher surface brightness objects in our sample (see Figure 6).

6. Summary and Outlook

In this paper, we have presented our source detection pipeline and an initial catalog of sources from our ongoing search for extended LSBGs in the Wide layer of the HSC-SSP. We have carried out our search within the first (gri full depth) 200 deg^2 of the survey, which will extend to 1400 deg^2 upon completion. Since our focus is on angularly extended galaxies ($r_{\text{eff}} = 2.5\text{''}-14\text{''}$), our sample is likely dominated by low-redshift sources. We present a catalog of 781 LSBGs, where we define LSBGs in terms of mean surface brightness ($\bar{\mu}_{\text{eff}}(g) > 24.3 \text{ mag arcsec}^{-2}$), as opposed to central surface brightness μ_0 , to allow nucleated galaxies into our sample. The contents of our catalog are summarized in Tables 1 and 2.

We divide our LSBG sample into red ($g - i \geq 0.64$) and blue ($g - i < 0.64$) galaxies, where the color boundary is at the median value. The surface brightness distributions ($\bar{\mu}_{\text{eff}}$ and μ_0) are strong functions of color, with the red distributions being much broader and generally fainter than that of the blue LSBGs (Figure 6); the median $\bar{\mu}_{\text{eff}}(g)$ and $\mu_0(g)$ for red LSBGs are 25.8 and $24.9 \text{ mag arcsec}^{-2}$, respectively, whereas they are 24.8 and $24.0 \text{ mag arcsec}^{-2}$ for blue LSBGs. Furthermore, this

trend shows a clear correlation with galaxy morphology (Figure 4). The surface brightness profiles of the red galaxies are typically very smooth and well characterized by single-component Sérsic functions (with median index $n = 0.9$). Their morphologies and apparent clustering with galaxy groups (Figures 5 and 11) suggest that they are composed of a combination of early-type dwarfs and UDGs in group environments—redshifts are required to distinguish between these possibilities for individual objects. In contrast, the blue galaxies tend to have irregular morphologies and show evidence of ongoing star formation.

We cross-match our sample with archival data to gain insight into the physical nature of the LSBGs (Section 5). We find that our sample encompasses a wide range of physical properties. From early-type dwarfs to star-forming LSB spirals, our LSBGs span at least a factor of ~ 20 and ~ 2000 in physical effective radius and optical luminosity, respectively (Figure 12). Nearly half (46%) of the galaxies in our sample (166 of which are blue) fall within the ALFALFA survey footprint; however, only three blue LSBGs have an H I counterpart in the 70% ALFALFA catalog (Section 5.1.3). Many of the blue LSBGs (296 out of 390), as well some of the red LSBGs (78 out of 391), have UV detections in the *GALEX* source catalog (Section 5.1.4 and Tables 1 and 2).

We note that we do not yet know the full redshift distribution (and thus the true surface brightness distribution) of our sample. However, our minimum size cut at $r_{\text{eff}} = 2.5\text{''}$ strongly biases our search to low-redshift sources. Consistent with this expectation, the redshifts we currently have in hand suggest a distance distribution with a range of ~ 30 –100 Mpc (Section 5). In addition, a preliminary clustering analysis to be published in a future work yields a consistent, nearby distance distribution. Nevertheless, it is possible that a small fraction of objects in our sample may be normal surface brightness to HSB sources at higher redshifts ($z \gtrsim 0.1$), where cosmological dimming begins to become non-negligible. However, our sample pushes to very low central surface brightnesses, and as a result, even if our *entire* sample is at $z = 0.1$ (which would imply that all sources have $r_{\text{eff}} > 4.6$ kpc), $>93\%$ of our sources would have $\mu_0(g) > 22 \text{ mag arcsec}^{-2}$ after correcting for cosmological dimming. It is, therefore, likely that the vast majority of galaxies in our catalog are true LSBGs.

The HSC-SSP is ushering in a new era for the study of LSBGs, which is currently the best preparation we have for the even deeper and wider imaging that will be produced by LSST. We consider this work a first step in the longer-term goal of building a statistical sample of ultra-LSB galaxies within the complete HSC-SSP footprint. As such, we have not yet pushed the data as far as they can go. For example, the sensitivity of our pipeline may be significantly improved with a multiscale approach such as wavelet decomposition (e.g., Prescott et al. 2012), or with new LSB-optimized background-subtraction and/or shape-measurement algorithms. Both our current and future search methods may also be applied to the Deep and Ultra-Deep layers of HSC-SSP, which have limiting magnitudes that are ~ 1 and 2 mag deeper than that of the Wide layer (over much smaller areas of sky). Nevertheless, our current LSBG catalog already demonstrates the potential of the HSC-SSP to deliver a truly unprecedented view of the galaxy population at low surface brightnesses.

Galaxies in the ultra-LSB regime represent a unique testing ground for theoretical predictions of galaxy and star formation,

stellar feedback processes, and the distribution and nature of dark matter. The galaxy catalog presented in this work will facilitate follow-up efforts to study the physical properties and number densities of these elusive galaxies as a function of environment. Pushing such studies to lower surface brightnesses will be necessary to form a more complete census of the galaxy population, which will ultimately provide one of the strongest tests of the standard Λ CDM framework.

We thank David Spergel and Jim Gunn for useful discussions about the galaxies in our sample. J.P.G. thanks Jim Bosch and Paul Price for their assistance with the LSST codebase, Adrian Price-Whelan for general coding advice, and Semyeong Oh for useful conversations and for sharing data presented in Figure 7. J.P.G. was supported by the National Science Foundation partially under grant no. AST 1713828 and partially through the Graduate Research Fellowship Program under grant no. DGE 1148900.

The Hyper Suprime-Cam (HSC) collaboration includes the astronomical communities of Japan and Taiwan and Princeton University. The HSC instrumentation and software were developed by the National Astronomical Observatory of Japan (NAOJ), the Kavli Institute for the Physics and Mathematics of the Universe (Kavli IPMU), the University of Tokyo, the High Energy Accelerator Research Organization (KEK), the Academia Sinica Institute for Astronomy and Astrophysics in Taiwan (ASIAA), and Princeton University. Funding was contributed by the FIRST program from Japanese Cabinet Office, the Ministry of Education, Culture, Sports, Science and Technology (MEXT), the Japan Society for the Promotion of Science (JSPS), Japan Science and Technology Agency (JST), the Toray Science Foundation, NAOJ, Kavli IPMU, KEK, ASIAA, and Princeton University.

This paper makes use of software developed for the Large Synoptic Survey Telescope. We thank the LSST Project for making their code available as free software at <http://dm.lsst.org>.

The Pan-STARRS1 Surveys (PS1) have been made possible through contributions of the Institute for Astronomy, the University of Hawaii, the Pan-STARRS Project Office, the Max-Planck Society and its participating institutes, the Max Planck Institute for Astronomy, Heidelberg and the Max Planck Institute for Extraterrestrial Physics, Garching, Johns Hopkins University, Durham University, the University of Edinburgh, Queens University Belfast, the Harvard-Smithsonian Center for Astrophysics, the Las Cumbres Observatory Global Telescope Network Incorporated, the National Central University of Taiwan, the Space Telescope Science Institute, the National Aeronautics and Space Administration under grant no. NNX08AR22G issued through the Planetary Science Division of the NASA Science Mission Directorate, the National Science Foundation under grant no. AST-1238877, the University of Maryland, and Eotvos Lorand University (ELTE) and the Los Alamos National Laboratory.

Based in part on data collected at the Subaru Telescope and retrieved from the HSC data archive system, which is operated by Subaru Telescope and Astronomy Data Center, National Astronomical Observatory of Japan.

Some of the data presented in this paper were obtained from the Mikulski Archive for Space Telescopes (MAST). STScI is operated by the Association of Universities for Research in Astronomy, Inc., under NASA contract NAS5-26555. Support

for MAST for non-*HST* data is provided by the NASA Office of Space Science via grant NNX09AF08G and by other grants and contracts.

Software: *hugs* (<https://github.com/johnnygreco/hugs>) *astropy* (Astropy Collaboration et al. 2013), *numpy* (Van der Walt et al. 2011), *scipy* (<https://www.scipy.org>), *matplotlib* (Hunter 2007), *sqlalchemy* (<https://www.sqlalchemy.org>), *schwimmbad* (Price-Whelan & Foreman-Mackey 2017), *sfdmap* (<https://github.com/kbarbary/sfdmap>), *photutils* (Bradley et al. 2017).

Appendix

Low Surface Brightness False Positives

The deep imaging afforded by HSC-SSP is essential for detecting new LSBGs; however, it is also sensitive to other LSB phenomena such as Galactic cirrus emission and tidal debris from galaxy interactions. These LSB sources, while interesting in their own right, are common false positives in searches for LSBGs. In this appendix, we provide examples of these LSB sources in data from the HSC-SSP.

A.1. Galactic Cirrus

Optical scattered light from dust grains in the interstellar medium, so-called Galactic cirrus, has long been recognized to exist (Elvey & Roach 1937; Guhathakurta & Tyson 1989), even at high Galactic latitudes (Sandage 1976). Galactic cirrus can be a significant contaminant for extragalactic studies, particularly when the focus is LSBGs or diffuse stellar halos around massive galaxies (e.g., Duc et al. 2015). At the same time, the combination of optical imaging (which maps the cirrus on small $\sim 1''$ scales) with infrared/microwave observations of thermal emission (e.g., using *WISE* and/or *Planck*) is a powerful probe of the physics of the interstellar medium (e.g., Miville-Deschénes et al. 2016).

In general, Galactic cirrus is not a major source of contamination in our search for LSBGs. One exception is within the HSC-SSP field that covers right ascensions in the range $330^\circ < \alpha < 345^\circ$ (bottom right panel in Figure 5). This field contains several patchy regions with large amounts of optical cirrus, which have a filamentary character with structures that span $\sim 5'-10'$. In Figure 13, we show a *gr-i*-composite image of an example of Galactic cirrus within this field. Given the characteristic wispy structure of Galactic cirrus and that cirrus clouds are often found within large networks of similar clouds, it is generally straightforward to eliminate such sources from our sample during our visual inspection step.

A.2. Tidal Debris

At the depths of HSC-SSP, galaxy interactions produce rich networks of LSB substructure and tidal debris, as predicted by the Λ CDM cosmological framework (Bullock & Johnston 2005; Johnston et al. 2008; Cooper et al. 2010). Therefore, the HSC-SSP data set offers the opportunity to study the buildup of massive stellar halos across environments via large samples of faint tidal features (e.g., Atkinson et al. 2013). Such studies have the potential to constrain the mass assembly rate of galaxies (van Dokkum 2005; Tal et al. 2009) and probe the orbital distributions of infalling satellite galaxies (Hendel & Johnston 2015) throughout the universe. We will use HSC-SSP to study LSB tidal features in future work (E. Kado-Fong et al. 2018, in preparation).

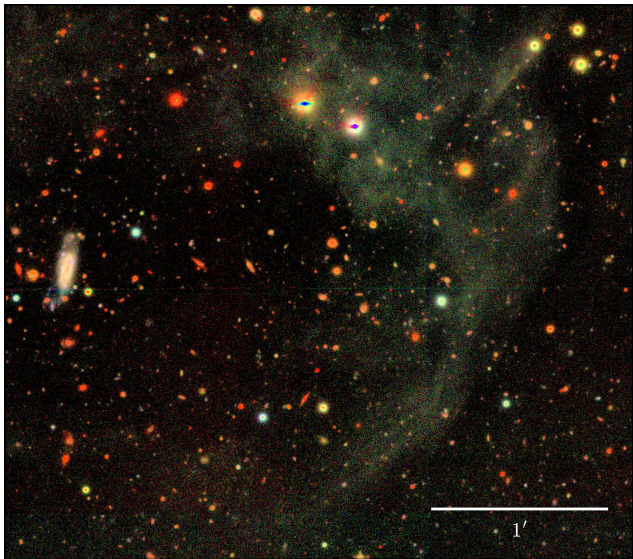


Figure 13. HSC-SSP *gri*-composite image of Galactic cirrus. Arising from the scattering of optical light off dust grains within the Milky Way, cirrus can be a source of contamination for extragalactic studies, even at high Galactic latitudes. The image is centered on $(\alpha, \delta) = (332^\circ 5903, -0^\circ 516959)$, with north up and east to the left.

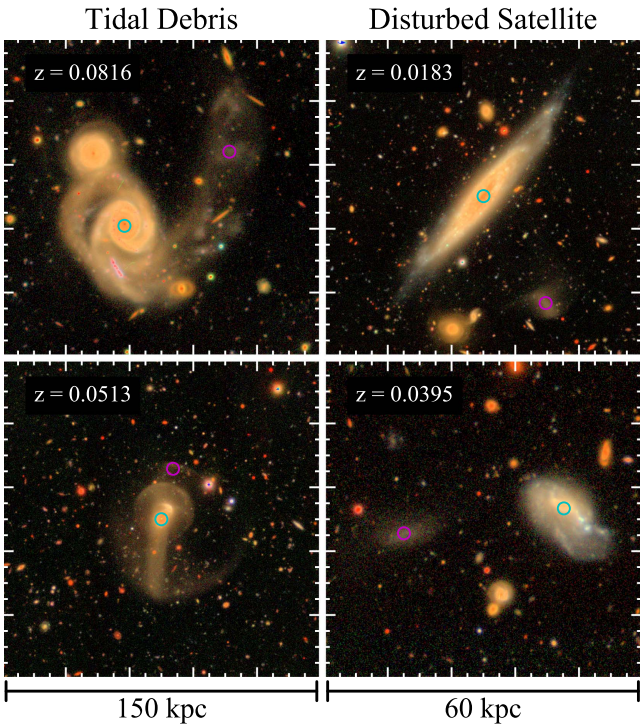


Figure 14. HSC-SSP *gri*-composite images of tidal debris (left column) and disturbed satellites (right column); note that the distinction between these types of LSB sources can be highly ambiguous. The sources detected by our pipeline are indicated by the magenta circles, and the likely host galaxies are indicated by the cyan circles. The physical scale for each column is shown on the bottom, where each panel assumes the redshift of the host galaxy indicated in the upper left corner.

Step 1 of our pipeline makes our search sensitive to LSB structures that are relatively isolated from HSB sources. As a result, a subset of objects detected by our pipeline may be tidal debris from galaxy interactions, which have been ejected far enough away from the primary system to have a distinct footprint in our segmented detection images. We attempt to

identify and remove such sources during the visual inspection step of our pipeline; however, there are inevitably ambiguous cases. For example, some objects might be better classified as tidally disturbed satellites rather than debris, and others may in fact be foreground dwarf galaxies with irregular morphologies. For a particularly interesting example of such an ambiguous case, see Greco et al. (2018).

In Figure 14, we show *gri*-composite images of two objects we classified as tidal debris (i.e., they are not in our final catalog; left column) and two we classified as disturbed satellites (i.e., they are LSBGs in our final sample; right column). We generally err on the side of including possible tidal debris in the sample.

ORCID iDs

Johnny P. Greco  <https://orcid.org/0000-0003-4970-2874>
 Michael A. Strauss  <https://orcid.org/0000-0002-0106-7755>
 Song Huang  <https://orcid.org/0000-0003-1385-7591>
 Ji Hoon Kim  <https://orcid.org/0000-0002-1418-3309>
 Alexie Leauthaud  <https://orcid.org/0000-0002-3677-3617>
 Robert H. Lupton  <https://orcid.org/0000-0003-1666-0962>
 Cristóbal Sifón  <https://orcid.org/0000-0002-8149-1352>

References

Abraham, R. G., & van Dokkum, P. G. 2014, *PASP*, **126**, 55
 Aihara, H., Allende Prieto, C., An, D., et al. 2011, *ApJS*, **193**, 29
 Aihara, H., Arimoto, N., Armstrong, R., et al. 2018a, *PASJ*, **70**, S4
 Aihara, H., Armstrong, R., Bickerton, S., et al. 2018b, *PASJ*, **70**, S8
 Akhlaghi, M., & Ichikawa, T. 2015, *ApJS*, **220**, 1
 Amorisco, N. C., & Loeb, A. 2016, *MNRAS*, **459**, L51
 Astropy Collaboration, Robitaille, T. P., Tollerud, E. J., et al. 2013, *A&A*, **558**, A33
 Atkinson, A. M., Abraham, R. G., & Ferguson, A. M. N. 2013, *ApJ*, **765**, 28
 Axelrod, T., Kantor, J., Lupton, R. H., & Pierfederici, F. 2010, *Proc. SPIE*, **7740**, 774015
 Baldry, I. K., Glazebrook, K., Brinkmann, J., et al. 2004, *ApJ*, **600**, 681
 Barbary, K. 2016, *JOSS*, **1**, 58
 Barden, M., Häußler, B., Peng, C. Y., McIntosh, D. H., & Guo, Y. 2012, *MNRAS*, **422**, 449
 Beijersbergen, M., de Blok, W. J. G., & van der Hulst, J. M. 1999, *A&A*, **351**, 903
 Bell, E. F., McIntosh, D. H., Katz, N., & Weinberg, M. D. 2003, *ApJS*, **149**, 289
 Bellazzini, M., Belokurov, V., Magrini, L., et al. 2017, *MNRAS*, **467**, 3751
 Bertin, E., & Arnouts, S. 1996, *A&AS*, **117**, 393
 Bertschinger, E. 1985, *ApJS*, **58**, 39
 Bianchi, L., Shiao, B., & Thilker, D. 2017, *ApJS*, **230**, 24
 Blanton, M. R., Kazin, E., Muna, D., Weaver, B. A., & Price-Whelan, A. 2011, *AJ*, **142**, 31
 Blanton, M. R., Lupton, R. H., Schlegel, D. J., et al. 2005, *ApJ*, **631**, 208
 Blanton, M. R., & Moustakas, J. 2009, *ARA&A*, **47**, 159
 Bosch, J., Armstrong, R., Bickerton, S., et al. 2018, *PASJ*, **70**, S5
 Bothun, G., Impey, C., & McGaugh, S. 1997, *PASP*, **109**, 745
 Bothun, G. D., Impey, C. D., Malin, D. F., & Mould, J. R. 1987, *AJ*, **94**, 23
 Boylan-Kolchin, M., Bullock, J. S., & Kaplinghat, M. 2011, *MNRAS*, **415**, L40
 Bradford, J. D., Geha, M. C., & Blanton, M. R. 2015, *ApJ*, **809**, 146
 Bradley, L., Sipocz, B., Robitaille, T., et al. 2017, *astropy/photutils*: v0.4, doi:10.5281/zenodo.1039309
 Brodie, J. P., Romanowsky, A. J., Strader, J., & Forbes, D. A. 2011, *AJ*, **142**, 199
 Bruzual, G., & Charlot, S. 2003, *MNRAS*, **344**, 1000
 Budavári, T., Heinis, S., Szalay, A. S., et al. 2009, *ApJ*, **694**, 1281
 Bullock, J. S., & Johnston, K. V. 2005, *ApJ*, **635**, 931
 Cardelli, J. A., Clayton, G. C., & Mathis, J. S. 1989, *ApJ*, **345**, 245
 Conroy, C., & Bullock, J. S. 2015, *ApJL*, **805**, L2
 Cooper, A. P., Cole, S., Frenk, C. S., et al. 2010, *MNRAS*, **406**, 744
 Coupon, J., Czakon, N., Bosch, J., et al. 2018, *PASJ*, **70**, S7

Dalcanton, J. J., Spergel, D. N., Gunn, J. E., Schmidt, M., & Schneider, D. P. 1997a, *AJ*, **114**, 635

Dalcanton, J. J., Spergel, D. N., & Summers, F. J. 1997b, *ApJ*, **482**, 659

Dark Energy Survey Collaboration, Abbott, T., Abdalla, F. B., et al. 2016, *MNRAS*, **460**, 1270

de Jong, J. T. A., Verdoes Kleijn, G. A., Boxhoorn, D. R., et al. 2015, *A&A*, **582**, A62

Disney, M. J. 1976, *Natur*, **263**, 573

Du, W., Wu, H., Lam, M. I., et al. 2015, *AJ*, **149**, 199

Duc, P.-A., Cuillandre, J.-C., Karabal, E., et al. 2015, *MNRAS*, **446**, 120

Eigenthaler, P., & Zeilinger, W. W. 2010, *A&A*, **511**, A12

Elvey, C. T., & Roach, F. E. 1937, *ApJ*, **85**, 213

Erwin, P. 2015, *ApJ*, **799**, 226

Ferrarese, L., Côté, P., Cuillandre, J.-C., et al. 2012, *ApJS*, **200**, 4

Ferrero, I., Abadi, M. G., Navarro, J. F., Sales, L. V., & Gurovich, S. 2012, *MNRAS*, **425**, 2817

Filippenko, A. V., Li, W. D., Treffers, R. R., & Modjaz, M. 2001, in *ASP Conf. Ser. 246, IAU Coll. 183: Small Telescope Astronomy on Global Scales*, ed. B. Paczynski, W.-P. Chen, & C. Lemme (San Francisco, CA: ASP), 121

Fliri, J., & Trujillo, I. 2016, *MNRAS*, **456**, 1359

Fukugita, M., Nakamura, O., Okamura, S., et al. 2007, *AJ*, **134**, 579

Galaz, G., Herrera-Camus, R., Garcia-Lambas, D., & Padilla, N. 2011, *ApJ*, **728**, 74

Geha, M., Blanton, M. R., Masjedi, M., & West, A. A. 2006, *ApJ*, **653**, 240

Geha, M., Blanton, M. R., Yan, R., & Tinker, J. L. 2012, *ApJ*, **757**, 85

Geha, M., Wechsler, R. H., Mao, Y.-Y., et al. 2017, *ApJ*, **847**, 4

Giovanelli, R., Haynes, M. P., Kent, B. R., et al. 2005, *AJ*, **130**, 2598

Greco, J. P., Greene, J. E., Price-Whelan, A. M., et al. 2018, *PASJ*, **70**, S19

Guhathakurta, P., & Tyson, J. A. 1989, *ApJ*, **346**, 773

Haynes, M. P., Giovanelli, R., Martin, A. M., et al. 2011, *AJ*, **142**, 170

Hendel, D., & Johnston, K. V. 2015, *MNRAS*, **454**, 2472

Huang, S., Haynes, M. P., Giovanelli, R., & Brinchmann, J. 2012, *ApJ*, **756**, 113

Hunter, J. D. 2007, *CSE*, **9**, 90

Impey, C., & Bothun, G. 1997, *ARA&A*, **35**, 267

Impey, C., Bothun, G., & Malin, D. 1988, *ApJ*, **330**, 634

Impey, C. D., Sprayberry, D., Irwin, M. J., & Bothun, G. D. 1996, *ApJS*, **105**, 209

Irwin, M. J. 1985, *MNRAS*, **214**, 575

Ivezic, Z., Axelrod, T., Brandt, W. N., et al. 2008, *SerAJ*, **176**, 1

Javanmardi, B., Martinez-Delgado, D., Kroupa, P., et al. 2016, *A&A*, **588**, A89

Jester, S., Schneider, D. P., Richards, G. T., et al. 2005, *AJ*, **130**, 873

Johnston, K. V., Bullock, J. S., Sharma, S., et al. 2008, *ApJ*, **689**, 936

Jurić, M., Kantor, J., Lim, K., et al. 2015, arXiv:1512.07914

Kauffmann, G., White, S. D. M., & Guiderdoni, B. 1993, *MNRAS*, **264**, 201

Kennicutt, R. C., Jr. 1998, *ARA&A*, **36**, 189

Kim, J. H. 2007, PhD thesis, Univ. of Maryland

Klypin, A., Kravtsov, A. V., Valenzuela, O., & Prada, F. 1999, *ApJ*, **522**, 82

Kniazev, A. Y., Grebel, E. K., Pustilnik, S. A., et al. 2004, *AJ*, **127**, 704

Koda, J., Yagi, M., Yamanoi, H., & Komiyama, Y. 2015, *ApJL*, **807**, L2

Kron, R. G. 1980, *ApJS*, **43**, 305

Leisman, L., Haynes, M. P., Janowiecki, S., et al. 2017, *ApJ*, **842**, 133

Lintott, C. J., Schawinski, K., Slosar, A., et al. 2008, *MNRAS*, **389**, 1179

Lupton, R., Blanton, M. R., Fekete, G., et al. 2004, *PASP*, **116**, 133

Machacek, M. E., Jerius, D., Kraft, R., et al. 2011, *ApJ*, **743**, 15

Mahdavi, A., Trentham, N., & Tully, R. B. 2005, *AJ*, **130**, 1502

Mandelbaum, R., Miyatake, H., Hamana, T., et al. 2018, *PASJ*, **70**, S25

Marino, A., Mazzei, P., Rampazzo, R., & Bianchi, L. 2016, *MNRAS*, **459**, 2212

Martin, D. C., Fanson, J., Schiminovich, D., et al. 2005, *ApJL*, **619**, L1

Martínez-Delgado, D., Gabany, R. J., Crawford, K., et al. 2010, *AJ*, **140**, 962

Martínez-Delgado, D., Lásker, R., Sharina, M., et al. 2016, *AJ*, **151**, 96

Mateo, M. L. 1998, *ARA&A*, **36**, 435

McConnachie, A. W. 2012, *AJ*, **144**, 4

McGaugh, S. S. 1996, *MNRAS*, **280**, 337

McGaugh, S. S., Bothun, G. D., & Schombert, J. M. 1995a, *AJ*, **110**, 573

McGaugh, S. S., Schombert, J. M., & Bothun, G. D. 1995b, *AJ*, **109**, 2019

Ménard, B., Scranton, R., Schmidt, S., et al. 2013, arXiv:1303.4722

Merritt, A., van Dokkum, P., Danieli, S., et al. 2016, *ApJ*, **833**, 168

Mihos, J. C., Durrell, P. R., Ferrarese, L., et al. 2015, *ApJL*, **809**, L21

Miville-Deschénes, M.-A., Duc, P.-A., Marleau, F., et al. 2016, *A&A*, **593**, A4

Miyazaki, S., Komiyama, Y., Kawanomoto, S., et al. 2018, *PASJ*, **70**, S1

Moore, B., Quinn, T., Governato, F., Stadel, J., & Lake, G. 1999, *MNRAS*, **310**, 1147

Mulchaey, J. S., Davis, D. S., Mushotzky, R. F., & Burstein, D. 2003, *ApJS*, **145**, 39

Muñoz, R. P., Eigenthaler, P., Puzia, T. H., et al. 2015, *ApJL*, **813**, L15

Oke, J. B., & Gunn, J. E. 1983, *ApJ*, **266**, 713

O’Neil, K., Bothun, G. D., Schombert, J., Cornell, M. E., & Impey, C. D. 1997, *AJ*, **114**, 2448

Papastergis, E., Adams, E. A. K., & Romanowsky, A. J. 2017, *A&A*, **601**, L10

Papastergis, E., Giovanelli, R., Haynes, M. P., & Shankar, F. 2015, *A&A*, **574**, A113

Prescott, M. K. M., Dey, A., & Jannuzzi, B. T. 2012, *ApJ*, **748**, 125

Price-Whelan, A. M., & Foreman-Mackey, D. 2017, *JOSS*, **2**, 357

Rix, H.-W., Barden, M., Beckwith, S. V. W., et al. 2004, *ApJS*, **152**, 163

Roberts, S., Davies, J., Sabatini, S., et al. 2004, *MNRAS*, **352**, 478

Rodríguez, S., & Padilla, N. D. 2013, *MNRAS*, **434**, 2153

Román, J., & Trujillo, I. 2017a, *MNRAS*, **468**, 703

Román, J., & Trujillo, I. 2017b, *MNRAS*, **468**, 4039

Rosenbaum, S. D., Krusch, E., Bomans, D. J., & Dettmar, R.-J. 2009, *A&A*, **504**, 807

Sandage, A. 1976, *AJ*, **81**, 954

Sandage, A., & Binggeli, B. 1984, *AJ*, **89**, 919

Schlafly, E. F., & Finkbeiner, D. P. 2011, *ApJ*, **737**, 103

Schlegel, D. J., Finkbeiner, D. P., & Davis, M. 1998, *ApJ*, **500**, 525

Schombert, J. M., McGaugh, S. S., & Eder, J. A. 2001, *AJ*, **121**, 2420

Sérsic, J. L. 1968, *Atlas de Galaxias Australes* (Cordoba, Argentina: ESO)

Sifón, C., van der Burg, R. F. J., Hoekstra, H., Muzzin, A., & Herbonnet, R. 2018, *MNRAS*, **473**, 3747

Sprayberry, D., Impey, C. D., Bothun, G. D., & Irwin, M. J. 1995, *AJ*, **109**, 558

Strateva, I., Ivezić, Z., Knapp, G. R., et al. 2001, *AJ*, **122**, 1861

Stritzinger, M., & Morrell, N. 2009, *CBET*, **1703**, 1

Tal, T., van Dokkum, P. G., Nelan, J., & Bezanson, R. 2009, *AJ*, **138**, 1417

Tonry, J. L., Dressler, A., Blakeslee, J. P., et al. 2001, *ApJ*, **546**, 681

Trentham, N., Tully, R. B., & Verheijen, M. A. W. 2001, *MNRAS*, **325**, 385

Trujillo, I., & Fliri, J. 2016, *ApJ*, **823**, 123

Tully, R. B. 1987, *ApJ*, **321**, 280

van der Burg, R. F. J., Hoekstra, H., Muzzin, A., et al. 2017, *A&A*, **607**, A79

van der Burg, R. F. J., Muzzin, A., & Hoekstra, H. 2016, *A&A*, **590**, A20

Van der Walt, S., Colbert, S. C., & Varoquaux, G. 2011, *CSE*, **13**, 22

van Dokkum, P., Abraham, R., Brodie, J., et al. 2016, *ApJL*, **828**, L6

van Dokkum, P. G. 2005, *AJ*, **130**, 2647

van Dokkum, P. G., Abraham, R., Merritt, A., et al. 2015, *ApJL*, **798**, L45

Wyder, T. K., Martin, D. C., Schiminovich, D., et al. 2007, *ApJS*, **173**, 293

Yagi, M., Koda, J., Komiyama, Y., & Yamanoi, H. 2016, *ApJS*, **225**, 11

Yang, X., Mo, H. J., van den Bosch, F. C., et al. 2007, *ApJ*, **671**, 153

York, D. G., Adelman, J., Anderson, J. E., Jr., et al. 2000, *AJ*, **120**, 1579

Zhong, G. H., Liang, Y. C., Liu, F. S., et al. 2008, *MNRAS*, **391**, 986

Zinn, P.-C., Stritzinger, M., Braithwaite, J., et al. 2012, *A&A*, **538**, A30

Zucker, D. B., Belokurov, V., Evans, N. W., et al. 2006, *ApJL*, **643**, L103